UNIVERISTY OF CALIFORNIA

Los Angeles

Next Generation Acoustic and Magnetic Devices for Radio Frequency Communication

A dissertation submitted in partial satisfaction of the requirements for the degree Doctor of Philosophy in Mechanical Engineering

by

Joseph Devin Schneider

2020

ABSTRACT OF THE DISSERTATION

Next Generation Acoustic and Magnetic Devices for Radio Frequency Communications

by

Joseph Devin Schneider

Doctor of Philosophy in Mechanical Engineering

University of California, Los Angeles, 2020

Professor Gregory P. Carman, Chair

This dissertation primarily focuses on utilizing low wave speed acoustic waves coupled with electromagnetics to increase performance of radio frequency front end architectures and reduce device dimensions. Chapter 1 begins with the history of communication technology beginning with Maxwell's equations. Next brief introductions into the piezoelectricity, magnetism, and multiferroics are given to lay the groundwork for the following Chapters.

Chapter 2 of this dissertation aims at improving the capability of communicating in lossy RF-denied media such as seawater. First, magnetic antennas are theoretically analyzed and compared to electric antennas showing that magnetic antennas perform better when surrounded by lossy conductive media. Next, a prototype multiferroic antenna is developed that uses piezoelectric PZT and magnetostrictive FeGa. The PZT applies a time varying stress to the FeGa causing the FeGa's internal flux density to dynamically vary resulting in a time-varying magnetic near field. Magnetic near field measurements are compared to an analytical model showing good agreement.

In Chapter 3 Lamb wave devices are investigated for filtering and frequency conversion applications in RF-front ends. Leveraging micro-fabrication techniques two Lamb wave delay lines are fabricated out of piezoelectric aluminum nitride (AlN). Interdigitated transducers (IDTs) are used to launch and receive Lamb waves as well as generate a time and space varying mechanical compliance. A circuit model is developed to compare to the experimental results and

determine the magnitude of the compliance nonlinearity present in the AlN. Results show that acoustic devices can be developed that simultaneously filter and down-convert or up-convert a signal.

Chapter 4 numerically analyzes strain tunable magnetic filters for applications in software defined radio and cognitive radio. For these applications filters with a tunable bandpass are necessary. The design relies on two CoFeB ellipses deposited on piezoelectric PMN-PT. An electric field is applied through the thickness of the PMN-PT resulting in a strain applied to the CoFeB ellipses. The electric field can be applied to either strain one ellipse or both ellipses. Straining both ellipses results in a tunable susceptibility from 6 GHz to 8 GHz, while straining only one ellipse results in a broadening of the bandpass response. These results show a potential solution for dynamic filters for next generation communication architectures.

The dissertation of Joseph Devin Schneider is approved.

Robert N. Candler

Ajit K. Mal

Yuanxun Wang

Gregory P. Carman, Committee Chair

University of California, Los Angeles

2020

For my family and friends.

Contents

List of Figures

List of Tables

VITA

Education:

2018 M.S. - Mechanical Engineering
University of California, Los Angeles

2015 B.S. - Mechanical Engineering
University of Louisville

Publications

The work presented in this thesis is based on the following publications and conference presentations

1. Joseph D. Schneider, John P. Domann, Paymon Shirazi, et al., "Experimental Demonstration and Operating Principles of a Multiferroic Antenna," J. Appl. Phys., vol. 126, no. 22, p. 224104, Dec. 2019

2. Joseph D. Schneider, Q. Wang, Y. Li, A. C. Chavez, J. Hu, and Greg Carman, "RF Voltage-Controlled Magnetization Switching in a Nano-Disk", J. Appl. Phys., vol. 126, no. 16, p. 163903, Oct. 2019

3. Joseph D. Schneider, John P. Domann, Paymon Shirazi, et al., "Experimental Demonstration and Operating Principles of a Multiferroic Antenna", Conference presentation, TANMS ARSM, January 2020

4. Joseph D. Schneider, Mohanchandra K. Panduranga, Taehwan Lee, Z. Xiao, et al., "Understanding the Magneto-Mechanical Response of Terfenol-D Micro/Nano-Structures",

MRS Fall Meeting, Magnetoelectrics II, Dec. 2019

5. Joseph D. Schneider, Katie Nygren, Qianchang Wang, Dominic Labanowski, Sayeef Salahuddin, Kristen Buchanan, and Greg Carman, "Acousticall Driven Magnetic Oscillations at High Frequency", SMASIS 2019, Multifunctional Materials 1, Sept. 2019

6. Joseph D. Schneider, John P. Domann, Paymon Shirazi, et al., "A piezoelectric driven magnetostrictive device for cmmunicating in the near field", SPIE Smart Structures and Materials + NDE and Health Monitoring, Mar. 2019

7. Joseph D. Schneider, Ting Lu, Greg Carman, Ethan Wang, and Ajit Mal, "Parametric coupling in Lamb wave devices", SPIE Smart Structures and Materials + NDE and Health Monitoring, Mar. 2019

8. Joseph D. Schneider, John P. Domann, Paymon Shirazi, et al., "Experimental and Numerical demonstration and validation of a Multiferroic Antenna at Low Frequencies", Conference presentation, MMM, Washington DC, January 2019

9. Joseph D. Schneider, Auni Kundu, Andres Chavez, Chris Lynch, and Greg Carman, "Creating Accessible Science Research Projects for High School and Undergraduate Students", Conference Presentation, XXVII International Materials Research Congress, Conference, Cancun Mexico, August 2018

10. Joseph D. Schneider, Qianchang Wang, D. Labanowski, Aryan Navabi, C. Chen, A. Sepulveda, Kang Wang, Sayeef Salahuddin, and Gregory P. Carman, "Acoustically Driven Spin Waves" Conference presentation, MMM, Pittsburgh, November 2017

1 Background and History

1.1 Introduction

Digital and wireless communications are the defining technologies of the past 100 years. They underpin the U.S. economy's largest companies, are crucial to coordinating the modern battle field, and are responsible for democratizing information for the average person. With increased user demand there is always motivation to increase the data rate and reduce the size of any device related to communications, whether it be the antenna or other crucial components such as mixers and filters. Furthermore, the frequency spectrum has recently become overcrowded resulting in the development of novel spectrum sensing approaches such as software defined radio and cognative radio. These methods require tunable RF filters that broaden and shift their operation frequency based on unused spectrum. For all of these reasons new types of filters, antennas, and mixers are highly desirable. In this Chapter, I will briefly go over some of the history of communication devices followed by introduction sections covering Piezoelectricity, Magnetism, and Multiferroics. I will end this Chapter with an overview of the rest of this dissertation.

1.1.1 History and Motivation

In 1861 and 1862 James Clerk Maxwell published an early form of what is now known as Maxwell's equations, given in differential form as [1].

$$\nabla \cdot \vec{E} = \frac{\rho}{\varepsilon_0} \tag{1.1}$$

$$\nabla \cdot \vec{B} = 0 \tag{1.2}$$

$$\nabla \times \vec{E} = -\frac{\partial \vec{B}}{\partial t} \tag{1.3}$$

$$\nabla \times \vec{B} = \mu_0 \vec{j} + \frac{1}{c^2} \frac{\partial \vec{E}}{\partial t} \tag{1.4}$$

where $\vec{E}$ and $\vec{B}$ are the electric and magnetic fields respectively. While ρ, ε_0, μ_0, c, and $\vec{j}$ are the charge density, permittivity of free space, permeability of free space, speed of light, and current density respectively. Maxwell subsequently used the above equations in 1965 to show that electric and magnetic fields travel through free space as waves at a constant velocity. Several years later, between 1886 and 1889, Heinrich Hertz, shown in Figure 1.1 (a), conducted a series of experiments proving that electromagnetic waves exist and thus proving Maxwell's theory. However, at the time Hertz did not realize the significance of his discovery and is quoted saying "*It's of no use whatsoever, this is just an experiment that proves Maestro Maxwell was right*". Since Hertz's discovery, his name was given to the fundamental unit for 1 over time and he is memorialized with several statues throughout the world, one of which is shown in Figure 1.1 (b).

(a)

(b)

Figure 1.1: (a) Photograph of Heinrich Hertz and (b) a statue of Heinrich Hertz memorializing his accomplishments in the field of electromagnetics. source: wikipedia Heinrich Hertz.

An additional major break through in communications in the invention of the superheterodyne receiver in the 1920s shown schematically in Figure 1.2. The superheterodyne receiver solved the problem of short wavelength amplification by down converting an incoming RF signal to an intermediate frequency (IF). The lower frequency at the IF stage allowed for more efficient amplification of the incoming signal. Figure 1.3 shows a photograph of a prototype superheterodyne receiver that used vacuum tubes for most of the amplification and frequency

mixing.

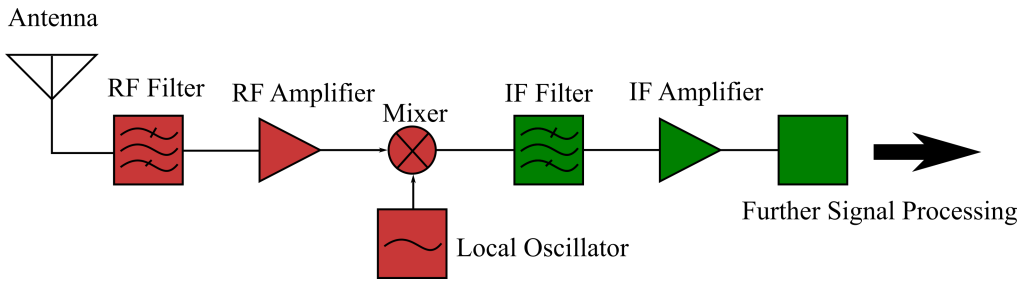

Figure 1.2: Schematic of a superheterodyne receiver. The antenna picks up a signal and then the signal is filtered, amplified, and mixed to a lower intermediate frequency (IF). Once the signal is down converted to the IF frequency it is filtered and amplified again for further signal processing.

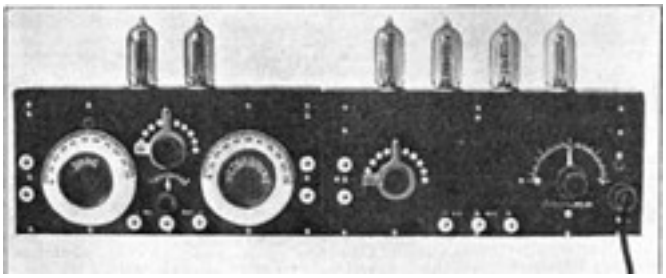

Figure 1.3: Photograph of a superheterodyne receiver. source: wikipedia superheterodyne receiver.

Until the invention of the interdigitated transducer (IDT) by White et.al. in 1965 [2], the filtering mechanism in RF receivers was carried out using resistors, inductors, and capacitors [3]. The IDT is used to launch acoustic waves in a single piezoelectric substrate. The advantage of using a single substrate allows for devices to be mass produced by leveraging microfabrication techniques. Furthermore, even in the early days of acoustic filters, to match their performance would have required hundreds of inductors and capacitors [3].

As mentioned previously, the superheterodyne receiver requires that the information carrying incoming wave to be down converted in frequency to the IF. One way achieve this frequency conversion is to use a nonlinear element such as a variable capacitor to create time and space varying material properties [4]. One recent approach is to use a mechanical nonlinearity, such as Compliance, to down convert the wave. The mechanical approach has two advantages: (1) the size of the acoustic device can be much smaller than the one presented in [4] because the acoustic wave speed is much slower than the electromagnetic wave speed, and (2) narrow

band devices can be created using IDTs resulting in the integration of filters and frequency conversion into a single component.

In the antenna space, one immediate application is communication in RF denied media such as seawater where frequencies on the order of 1 - 30 kHz are desirable because of their large skin depth [5]. These low frequencies correspond to large wavelengths resulting in antenna sizes on the order of a km. Furthermore, magnetic based antennas are known to have much better radiation characteristics when placed underwater or in conductive media [6]. The improved radiation from a magnetic based antenna comes from the fact that the magnitude of the electric field directly near an antenna is much smaller for the magnetic antenna than for the electric antenna. Thus, less power is dissipated in the conducting media when a magnetic antenna is used.

An approach to reduce the size of low frequency antennas is to use mechanical antennas [7–12] that use ferroelectric or ferromagnetic materials as the radiation mechanism. This is another situation where the use of low velocity acoustic waves are utilized to reduce the size of antennas.

1.2 Piezoelectricity

The prefix piezo is derived from the Greek word for press, thus the word piezoelectricity describes the linear interaction between mechanical and electrical systems. First discovered in 1880 by Jacques and Pierre Curie, piezoelectric materials have been ubiquitous in modern technology since the 1970s where they are used as filters for communication systems [3, 13, 14]. The invention of the interdigitated transducer (IDT) in 1965 [2] revolutionized the electronic filter. The IDT allowed the generation of surface acoustic waves (SAWs) at a narrow band frequency. The SAW technology replaced bulky inductors and capacitors that were previously used for the filter mechanism in superheterodyne receivers. As technology progressed,

filter mechanisms using bulk waves in AlN were developed [15]. Recently, researchers are exploring Lamb waves for filters because of their higher order modes which allow for higher operating frequencies [16].

The piezoelectric effect can be broken into two phenomenon, the direct effect and converse effect. The direct effect is when a mechanical stress induces an electrical polarization, whereas the converse effect is when an electric field induces a mechanical stress [17]. In this section the basic equations of piezoelectricity will be developed from thermodynamics followed by some examples of Finite Element Modeling to determine fundamental parameters for piezoelectric Lamb wave filters.

1.2.1 Thermodynamics of Piezoelectricity

Various forms of the constitutive equations describing piezoelectricity can be derived from thermodynamic energy functions. The choice of independent and dependent variable will determine the form of the constitutive equations obtained. In this section I will briefly go over one energy function and derive the constitutive equations. I recommend the textbook "Fundamentals of Piezoelectricity" by Takuro Ikeda for more information and derivations of the constitutive equations for piezoelectricity. The Electric Gibbs Energy function is given as

$$G(S,E) = \frac{1}{2}C^E S^2 - eSE - \frac{1}{2}\varepsilon^s E^2 \tag{1.5}$$

where C^E is the stiffness at constant electric field, S is the strain, E is the electric field, ε is the permittivity at constant strain, and e is the piezoelectric coupling constant. Here, the strain and electric field are the independent variables. Other energy functions in terms of different independent variables can be derived by performing the Legendre Transform on the Gibbs Energy. Note that the material properties above are tensor quantities, however, the indices have

been left out in this derivation. The total differential for the Gibbs Energy is

$$dG(S,E) = \frac{\partial G}{\partial S}dS - \frac{\partial G}{\partial E}dE \tag{1.6}$$

where the first differential is the stress (T) and the second differential is the electric displacement field (D). From these definitions the T and D are given as

$$T = C^E S - eE \tag{1.7}$$

$$D = eS + \varepsilon^s E \tag{1.8}$$

Equations 1.7 and 1.8 are the piezoelectric constitutive equations in stress-charge form. Specifically, Equation 1.7 describes the change in stress due to an applied strain and an applied electric field while Equation 1.8 describes the change in electric displacement field due to an applied electric field as well as an applied strain.

1.2.2 Finite Element Modeling and Experimentation of High Frequency Piezoelectricity

In engineering, specifically when designing a device, it is important to understand the metrics defined for characterizing the device's performance (i.e. figures of merit). For acoustic filters used in communications one of the major figures of merit (FOM) is transmission coefficient. The transmission coefficient for a two port device can be described in terms of a scattering parameter (s-parameter) defined as

$$S_{21} = \frac{V_2}{V_1}. \tag{1.9}$$

Equation 1.9 describes the voltage received at port 2 when an incident voltage wave is inputted into port 1. S-parameters are measured using a Vector Network Analyzer which is shown in Figure 1.4.

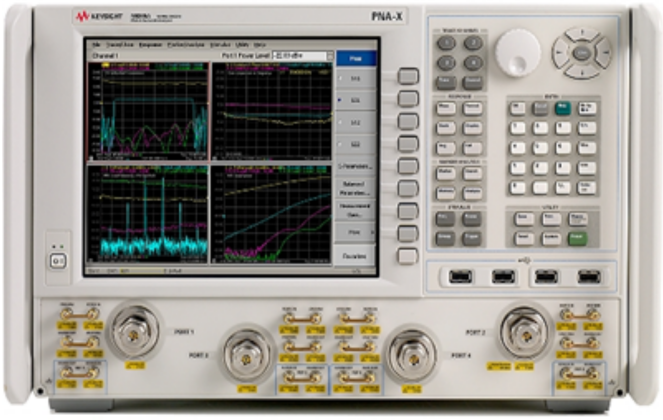

Figure 1.4: Vector Network Analyzer used to measure scattering parameters

Before fabricating a device a design process using various forms of modeling is typically implemented. Using modeling techniques, large numbers of device designs can be modeled and optimized. This modeling first approach saves time and money due to the high cost of prototyping using CMOS fabrication techniques. Modern finite element methods (FEMs) offer the ability to numerically model fully coupled piezoelectric and acoustic devices. For this subsection I will describe the modeling of Lamb wave delay lines. Note that Chapter 3 covers Lamb wave devices.

Figure 1.5 shows a schematic of a Lamb wave delay line. Lamb waves are acoustic waves that travel parallel to the surfaces of a plate with finite thickness [18]. It is assumed that the lateral dimensions of the plate are large compared to its thickness H and both (top and bottom) surfaces are traction free. H. Lamb in his classic paper showed that the solution of the equation motion satisfying the boundary conditions results in two sets of guided waves in the plate with symmetry and antisymmetry about its midplane. Both of these waves are highly dispersive and can propagate relatively large distances along the plate in comparison with the so-called body waves These guided waves are called Lamb waves and their propagation characteristics in both isotropic and anisotropic plates have been studied in great detail. In particular, when the wavelengths of the elastic waves are long compared to H in the frequencies of interest, as is the case here, it has been shown that the speed of the symmetric waves approaches the value

c_p in the zero-frequency limit, given by

$$c_p = \sqrt{\frac{E_p}{\rho}}. \tag{1.10}$$

where

$$E_p = \frac{E}{1-\nu^2} \tag{1.11}$$

where E is the Elastic Modulus and ν is Poisson's Ratio of the material Moreover, the dispersion curve for the fundamental or S_0 mode is almost flat at low frequencies. In addition, the displacement components associated with the waves in the S_0 mode satisfy the condition

$$|\frac{u_y}{u_x}| = O\left(\frac{\omega H}{c_p}\right) \tag{1.12}$$

where ω is the frequency and H is the plate thickness (Figure 1.5), implying that these waves are almost longitudinal at relatively low frequencies. It should be noted that the speed of the antisymmetric waves approaches zero in the limit of zero frequency and they are transverse and highly dispersive at low frequencies.

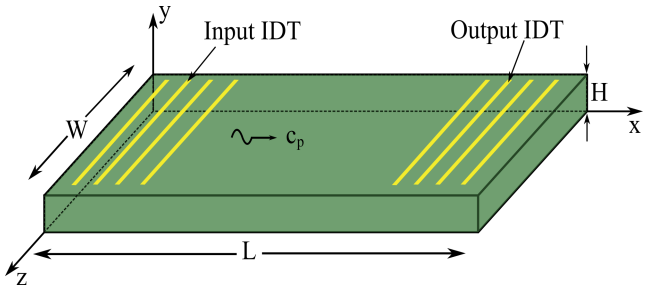

Figure 1.5: A schematic of a Lamb wave delay line built on Aluminum Nitride. The input IDT is used to launch acoustic waves in the x-direction, while the output IDT receives the incoming acoustic wave. Note that for these devices, the thickness H is much smaller than an acoustic wavelength.

The Lamb wave delay line was modeled in 2-dimensions using a fully coupled FEM package in frequency domain. A 400 nm Aluminum Nitride (AlN) thin film is the piezoelectric material that the wave travels in. The Lamb wave is launched using an input IDT and received using an output IDT both made with 100 nm of Al. Each IDT is composed of 15 signal fingers and 15 grounded fingers. The IDTs are separated by 0.6 mm. The input IDT launches acoustic

waves in both directions, thus, a perfectly matched layer is used to absorb the wave launch in the opposite direction to the receive IDT. Platinum (Pt) is placed on the bottom surface of the AlN only directly under the IDTs. Figure 3.1 (b) shows a schematic of the model. A frequency domain simulation is performed to determine the transmission coefficient (S_{21}).

Figure 1.6 shows the transmission coefficient (S21) for the Lamb wave delay line. The red dashed line is the numerical result from FEM modeling while the solid black line is experimentally measured data from a Lamb wave delay line with the same dimensions as the modeled device. The model and experimental data closely match with the main pass-band being from 415 MHz to approximately 470 MHz. The ripples at the peak of the pass-band are due to spurious acoustic modes present in the AlN. The pass-band is approximately 5-10 MHz larger for the experimental data due to the contact pads used to input the electrical signal into the IDTs. Regardless, the model closely matches the experimental data showing that FEM is a viable solution to model piezoelectric acoustic devices.

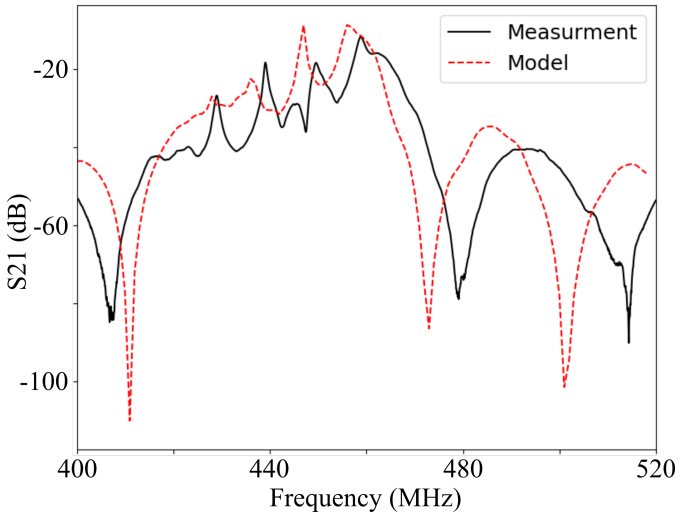

Figure 1.6: The S21 (i.e. insertion loss) for a Lamb wave device designed for a 460 MHz center frequency. The dashed red line is the results from the FEM model while the solid black line is the experimental results from a fabricated Lamb wave device.

Figure 1.7 shows the displacement from finite element simulations of a Lamb Wave device (a) and a surface acoustic wave (SAW) device (b) for comparison. In both plots, the color represents the magnitude of the particle displacement. The thickness of the material for the Lamb wave device is 400 nm which is much thinner than an acoustic wavelength. Furthermore, the ar-

rows indicate the direction of the displacement, indicating that the majority of the displacement is collinear with the direction of wave propagation as predicted by Equation 1.12. However, for the SAW device, the thickness is 0.5 mm which is much thicker than an acoustic wavelength. Additionally, for the SAW device the displacement is mostly contained at the surface of the material and the particle displacement profile is elliptical.

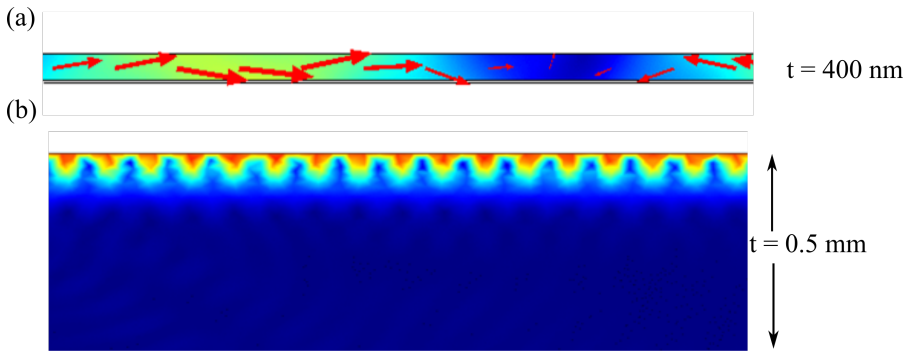

Figure 1.7: Fully coupled Finite Element Method simulation of acoustic wave devices. (a) Lamb wave device where the wave is propagating from left to right, the color represents the magnitude of the displacement while the arrows represent the direction. (b) Surface acoustic wave (SAW) device used as a comparison. Note that the wave is contained in the top portion of the device and the thickness of the material is much larger than the acoustic wavelength.

1.3 Magnetism

1.3.1 Introduction

To some extent, all materials are affected by a magnetic field. The properties of materials, related to magnetism, can be divided into five categories; diamagnetism, paramagnetism, ferromagnetism, ferrimagnetism, and antiferromagnetism. The most familiar category is ferromagnetism where a vector component of magnetic moments, from individual atoms or ions, are aligned. There are two primary contributors to this alignment, exchange energy and magnetocrystalline anisotropy, both of which are responsible for hard permanent magnets [19]. Figure 1.8 shows a permanent magnet surrounded by iron shavings. The iron shavings align with the field created from the magnet displaying the magnet's field pattern.

In this section some fundamental properties of magnetic materials will be discussed to better understand their physics and how they are used in technology. First the equation of motion without loss will be developed. The equation of motion will then be used to explain the phenomenon of ferromagnetic resonance and derive the corresponding equation (i.e Kittel's Equation) for a specific case. Lastly, magnetostriction will be briefly explored. Note, I will use classical mechanics to describe the relevant properties of magnetism. However, magnetism is quantum mechanical in nature and thus is best explained using quantum mechanics [19–21].

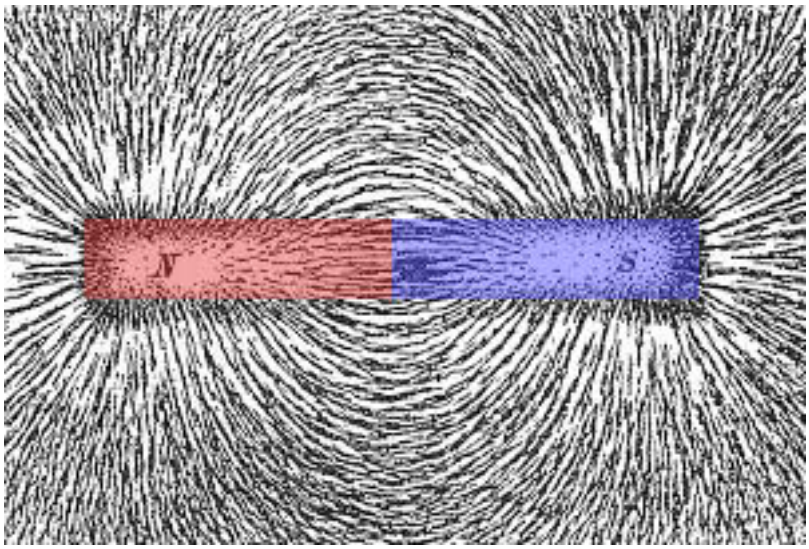

Figure 1.8: A permanent magnetic surrounded by iron shavings displaying the field pattern [https://www.explainthatstuff.com/magnetism.html].

1.3.2 Equation of Motion

Figure 1.9 shows a magnetic moment $\vec{m} = \gamma\vec{J}$ precessing about the z-axis in a steady magnetic flux density. Here, γ is the gyromagnetic ratio and $\vec{J}$ is the angular momentum. The magnetic flux density $\vec{B}$ results in a torque applied to $\vec{m}$. The torque is equal to the time rate of change of the angular momentum, thus the equation

$$\frac{d\vec{J}}{dt} = \gamma\vec{J} \times \vec{B} \tag{1.13}$$

is used to describe the time rate of change of the angular momentum. The magnetization of a material is the volume average of magnetic moments and is typically labeled as $\vec{M} = m/V$.

Replacing $\vec{J}$ in Equation 1.13 with $\vec{M}$ results in

$$\frac{d\vec{M}}{dt} = \gamma\mu_0\vec{M} \times \vec{H}_{eff} \tag{1.14}$$

where $\vec{H}_{eff}$ is the summation of the applied magnetic field and other effective fields in the system such as the magnetoelastic field and demagnetizing field. Equation 1.14 is the Landau-Lifshitz (LL) equation of motion for the magnetization without losses. The LL equation is a common starting point for the derivation of the ferromagnetic resonance (FMR) which describes the frequency of magnetization precession in a uniform applied magnetic field.

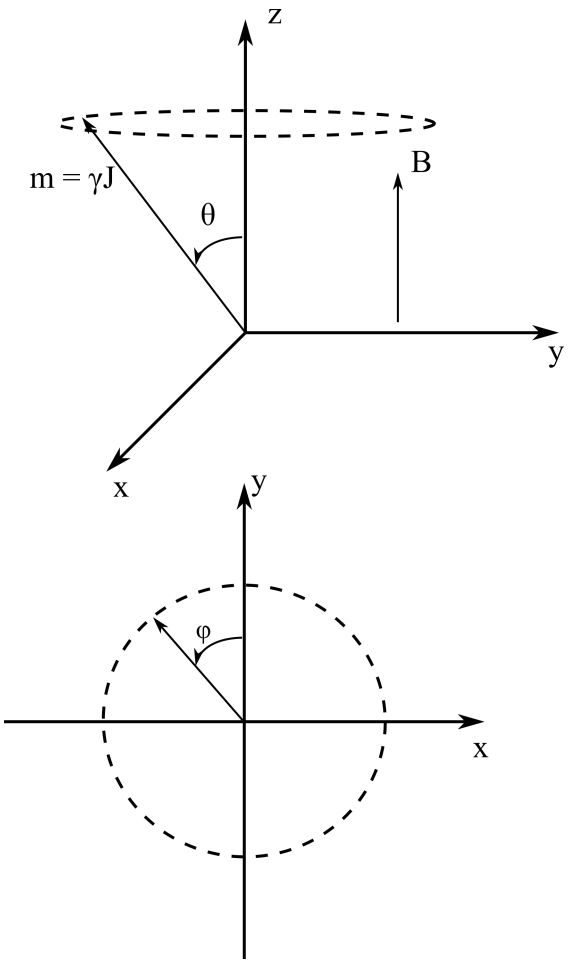

Figure 1.9: Precession of a magnetic moment in a DC flux density.

1.3.3 Ferromagnetic Resonance

Ferromagnetic resonance (FMR) is the defined as the uniform precessional motion of magnetic spins about an applied magnetic field (H_{app}) in a ferromagnetic sample [19, 22]. This can be visualized as an arrow, representing a single spin, precessing about the z-axis as is shown in Figure 1.9. The frequency of spin precession is the frequency at which electromagnetic energy is absorbed by the magnetic material. This absorption of energy is used in microwave components such as filters [5] and frequency selective limiters [23]. Furthermore, the precession causes the high frequency second rank magnetic susceptibility tensor to be nonsymmetric resulting in different properties in different directions. These nonsymmetric material properties are used to make nonreciprocal microwave components such a circulators and isolators [5]. The operating frequency of previously mentioned devices will depend on the FMR frequency of the magnetic sample. Thus, an equation to approximate this is very useful for initial device analysis.

Starting with Equation 1.14 the FMR frequency can be derived taking into account the shape of the magnetic material (i.e. demagnetization effects). A thin ellipse in the xy-plane is assumed and the long axis of the ellipse is along the x-axis. The total magnetic field including shape effects is written as

$$\vec{H}_{tot} = \left(H_{effx} - N_x M_x\right)\hat{x} + \left(H_{effy} - N_y M_y\right)\hat{y} + \left(H_{effz} - N_z M_z\right)\hat{z} \tag{1.15}$$

where N_x, N_y, and N_z are the demagnetizing factors and M is the magnetization component in the corresponding direction. Substituting Equation 1.15 into Equation 1.14 for the H_{eff} term results in the following three equations

$$\frac{\partial M_x}{\partial t} = -\gamma\left(M_y\left(H_{effz} - N_z M_z\right) - M_z\left(H_{effy} - N_y M_y\right)\right)\hat{x} \tag{1.16}$$

$$\frac{\partial M_y}{\partial t} = -\gamma\left(-M_x\left(H_{effz} - N_z M_z\right) + M_z\left(H_{effx} - N_x M_x\right)\right)\hat{y} \tag{1.17}$$

and

$$\frac{\partial M_z}{\partial t} = -\gamma\left(M_x\left(H_{effy} - N_y M_y\right) - M_y\left(H_{effx} - N_x M_x\right)\right)\hat{z} \tag{1.18}$$

if we assume that a strong external field is along the x-axis (i.e. long axis of the ellipse), Equation 1.16 is equal to 0. Taking Equations 1.17 and 1.18 and assuming sinusoidal variations in the magnetization results in the following two equations.

$$j\omega m_y + \gamma\left[H_{effx} + M_s(N_z - N_x)\right] m_z = 0 \tag{1.19}$$

$$j\omega m_z + \gamma\left[-H_{effx} + M_s(N_x - N_y)\right] m_y = 0 \tag{1.20}$$

Where M_s is the saturation magnetization of the magnetic material. Solutions to Equations 1.19 and 1.20 exist if the determinate of the system is 0 resulting Kittel's equation for ferromagnetic resonance [22]

$$\omega_{FMR} = \mu_0\gamma\sqrt{\left[Ms\,(N_x - N_z) - H_{effx}\right]\left[Ms\,(N_x - N_y) - H_{effy}\right]} \tag{1.21}$$

Equation 1.21 shows that the ferromagnetic resonance frequency of a magnetic material depends on the shape and effective magnetic fields H_{eff} in the sample which could be due to strain, magnetocrystalline anisotropy, and other effects. Figure 1.10 shows an example FMR plot. The color represents the percentage of electromagnetic energy absorbed by a thin film of ferromagnetic cobalt iron boron (CoFeB). It is easily seen in this figure that the FMR frequency is a function of applied magnetic field. This type of frequency tuning has applications in the fields of cognative radio and software defined radio where tunable filters are essential [24–26]. Here, by tuning the effective field using either a strain or an applied magnetic field the FMR frequency (i.e. frequency of a filter) can be tuned.

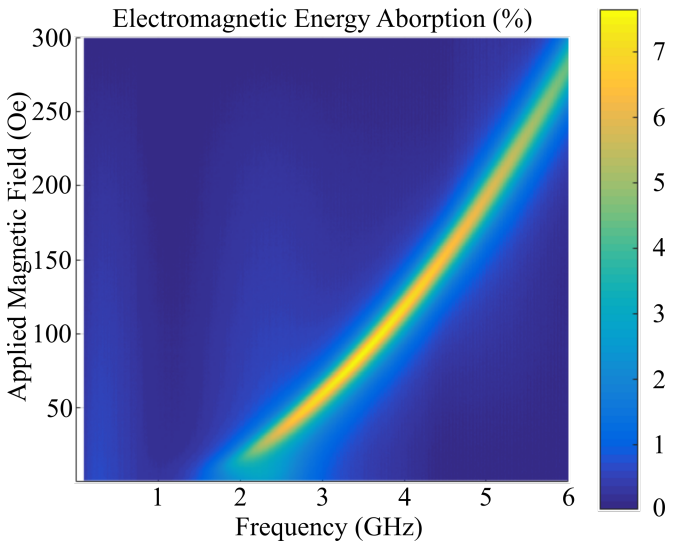

Figure 1.10: Ferromagnetic Resonance spectrum of a thin film of CoFeB. The color map shows the percentage of electromagnetic energy absorbed by the thin film as a function of frequency and applied magnetic field.

1.3.4 Magnetostriction

All ferromagnetic materials experience a change in geometry during the magnetization process. This change in geometry is termed magnetostriction. Conversily, if a magnetic material is strained, the internal magnetization changes. Magnetostriction was first discovered in 1847 by James Joule where he published his findings in his classic paper ”On the Effects of Magnetism upon the Dimensions of Iron and Steel Bars” [27]. Recently, the magnetostriction effect has been explored for antenna applications [6–9, 28, 29] (covered in Chapter 2), medical applications [30–34], radio frequency communications [26, 35], computing [36–43], and sensing [44–49].

Modeling of magnetostrictive elements has become relevant with this increase in applications and interest. One method used uses a Finite Difference Time Domain approach and includes a uniform uniaxial anisotropy to represent the magnetoelastic effective field H_{me}. The elastic energy in index notation is given as

$$E_{el} = \frac{1}{2} C_{ijkl} \varepsilon_{ij}^{el} \varepsilon_{kl}^{el} \tag{1.22}$$

where C_{ijkl} is the stiffness tensor and ε_{ij}^{el} is the strain tensor due to elasticity. The total strain is due to both magnetization changes and elastic changes (i.e. an applied stress). In the case considered here, a thin magnetostrictive ferromagnetic film is attached to a PMN-PT substrate similar to the case discussed in Chapter 4 creating a multiferroic composite. It is also assumed that the thin film is patterned into a structure such that the vector sum of the magnetization is approximately equal to the saturation magnetization M_s. In this case, the strain due the magnetization process is given as

$$\varepsilon^m = \frac{3}{2}\lambda_s \left(m^2 - \frac{1}{3} \right) \tag{1.23}$$

where λ_s is the saturation magnetostriction strain [50] and m is the normalized magnetic moment. The PMN-PT crystal cut used in Chapter 4 and considered in the analysis here strains in tension a long the x-axis while straining in compression in the y-axis when an electric field is applied through the thickness. Thus, the total change in energy is the difference between the energy change along the x-axis minus the energy change along the y-axis. Furthermore, the material is assumed to have isotropic homogeneous elastic properties, thus, C_{ijkl} reduces to just the elastic modulus E. The effective magnetic field due to magnetostriction is given as

$$H_{me} = -\frac{1}{\mu_0 M_s} \frac{\partial E_{el}}{\partial m} \tag{1.24}$$

substituting Equations 1.22 and 1.23 into Equation 1.24 results in

$$H_{me} = -\frac{3}{\mu_0 M_s} \lambda_s E \left(\varepsilon_{xx} - \varepsilon_{yy} \right) \tag{1.25}$$

Lastly, the uniaxial anisotropy can is calculated using

$$K_{me} = \frac{\mu_0 M_s H_{me}}{2}. \tag{1.26}$$

The above equation is used to input a strain induce uniaxial anisotropy in the governing equation for micromagnetics. The equation can then be solved for using a number of numerical methods, one example of this is the Finite Difference Time Domain method used in Chapter

4.

1.4 Multiferroics

Multiferroic materials are materials that contain more than one ferroic order. In the cases presented here (Chapters 2 and 4), linearized ferroelectricity and ferromagnetism are combined to form multiferroic heterostructures. Figure 1.11 shows a diagram explaining strain-coupled multiferroics. The left branch represents piezoelectricity while the right branch represents magnetostriction. Combining these materials in a composite allows for the control of magnetism with an electric field through stress and strain. One of major motivations for strain-coupled multiferroics is that strain mediated control of magnetism on the nanoscale is an energy efficient method for next generation magnetic computing technology.

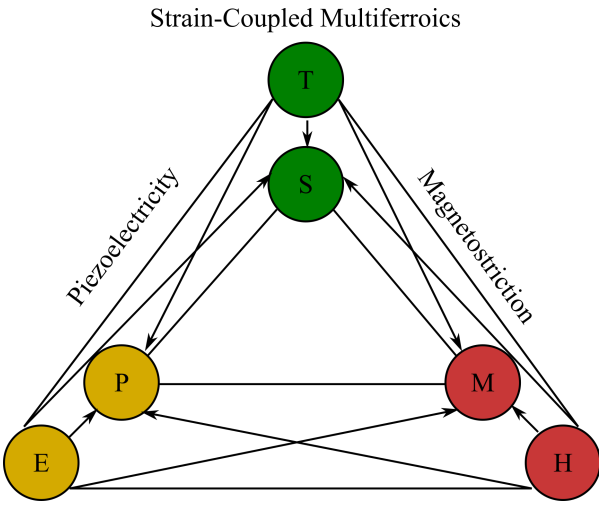

Figure 1.11: Diagram of strain-coupled multiferroics. The left branch represents piezoelectricity which is responsible for strain induced piezoelectricity. The right branch represents magnetostriction or magnetic field induced strain. Combining these elements results in the ability to control magnetization with an electric field.

Figure 1.12 shows an example of a multiferroic composite and its modeled operation mechanism [35]. Figure 1.12 (a) shows the structure being studied, a ferromagnetic 2 nm thick nanodisk is deposited onto piezoelectric PZT-5H along with two electrodes used to apply an electric field through the thickness of the PZT-5H. Figure 1.12 (b) shows the magnetization be-

fore an electric field is applied to the PZT-5H, note that the magnetization is out of plane in this scenario due to the perpendicular magnetic anisotropy (PMA) effect. Figure 1.12 (c) shows the magnetization and the path it took to reach equilibrium (blue line) after a voltage was applied. This is a perfect example of how strain, actuated through the piezoelectric effect, can be used to control magnetism on the nanoscale. Furthermore, this approach relies on a voltage as opposed to a current to switch the magnetization, therefore, Ohmic losses are avoided. It should be noted that all piezoelectrics in this configurations electrically act as capacitors so there will be some current draw when a voltage is applied. However, this current should be much lower than the currents required to generate an Oersted field large enough to switch the magnetization.

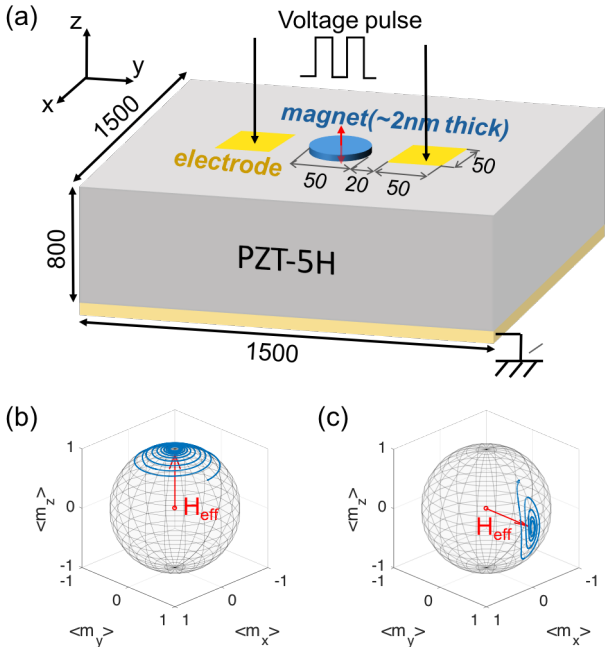

Figure 1.12: An example of a strain-coupled multiferroic device. (a) a 2 nm thick ferromagnetic nanodisk is deposited on top of piezoelectric PZT-5H. There are two electrodes for applying an electric field through the thickness of the PZT-5H. (b) The magnetization before a voltage is applied and (c) the magnetization after the voltage is applied. In both (b) and (c) the blue lines represent the path the magnetization took to equilibrium.

1.4.1 Acoustically Driven Magnetic Oscillations

Another example of a multiferroic device is the acoustically driven magnetic oscillations device as shown in Figure 1.13 [45, 46]. The device operates by using a high frequency strain from an acoustic wave in lithium niobate to drive magnetic oscillations in a ferromagnetic material

at the ferromagnetic resonance (FMR) frequency and at higher order spin wave modes. This is accomplished by using an IDT to launch a surface acoustic wave (SAW). The SAW propagates in the lithium niobate interacting with a nickel film to drive magnetic oscillations. This effect is measured by looking at the change in output power from an output IDT as a function of the magnetic bias field. These devices have applications for magnetic field measurements and efficient spin wave generation.

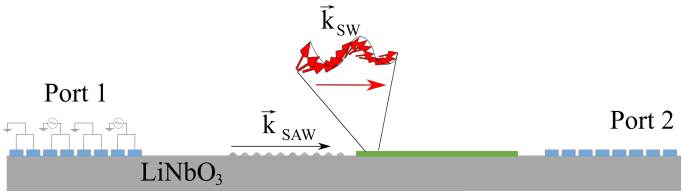

Figure 1.13: A diagram of an acoustically driven magnetic device. Two aluminum IDT sets and a nickel thin film are fabricated on the surface of piezoelectric 128 YX lithium niobate. An acoustic wave is launched from port 1 and power from the acoustic wave is absorbed into the nickel thin film. The remaining power in the acoustic wave is measured by the IDT connected to port 2.

Figure 1.14 shows an optical image of a SAW devices with a 300 x 300 μm nickel thin film (approximately 20 nm thick). The IDTs were fabricated by Dominic Labanowski while the rest of the devices was fabricated by Qianchang (QC) Wang. The IDTs are a double finger design (Figure 1.14) resulting in the ability to launch acoustic waves at the odd order harmonics. Thus, the fundamental frequency of this device is 600 MHz but here the focus is the 1.8 GHz frequency.

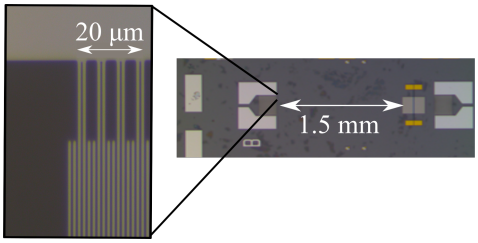

Figure 1.14: An optical image of an acoustically driven magnetic oscillations device. IDTs were fabricated by Dominic Labanowski and the rest of the device was fabricated by Qianchang (QC) Wang. Two IDT sets and a nickel thin film are fabricated on the surface of piezoelectric 128 YX lithium niobate. An acoustic wave is launched from port 1. Power from the acoustic wave is absorbed into the nickel thin film. The remaining power in the acoustic wave is measured by the IDT connected to port 2.

Figure 1.15 (a) shows the transmission coefficient (S21) of the device shown in figure 1.14.

The peaks in the plot represent frequencies where maximum power transmission occurs. The fundamental operating frequency is 600 MHz and the third order harmonic frequency is at 1.8 GHz and is labeled in the figure. Figure 1.15 (b) shows the transmission coefficient (S21) as a function of magnetic bias field operating at 1.8 GHz. The dips in transmission at plus and minus 50 Oe represent the bias field at which the acoustic energy is being absorbed into the nickel thin film through magnetoelastic coupling into the magnetic moments.

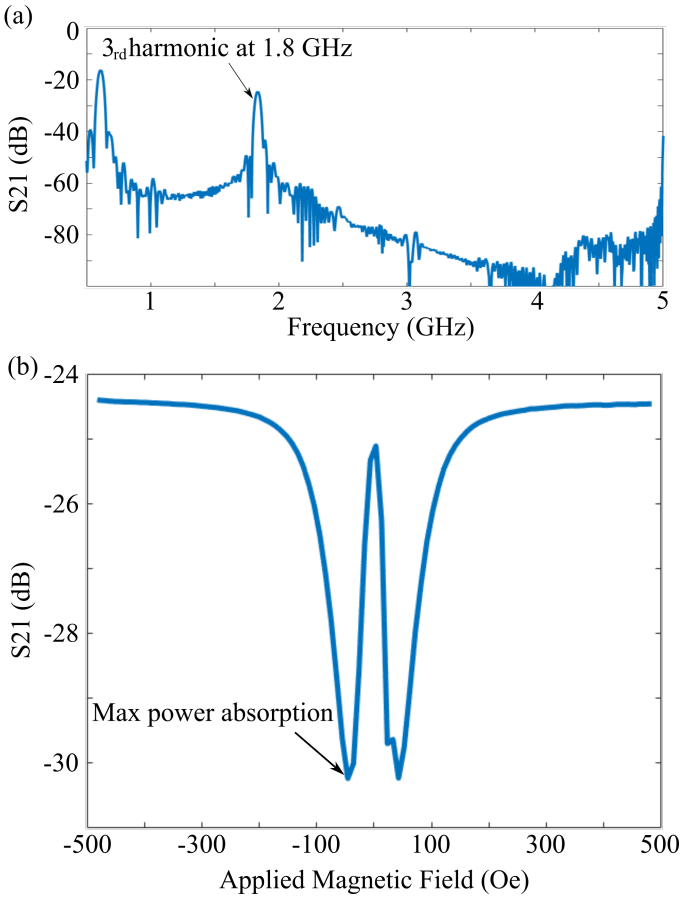

Figure 1.15: Results from the acoustically driven magnetic oscillations device. (a) The transmission coefficient from input IDT to output IDT as a function of frequency. The fundamental operating frequency is 600 MHz and the the third harmonic frequency is 1.8 GHz (labeled in the figure). (b) The transmission coefficient S21 at 1.8 GHz as a function of magnetic field. The maximum power absorption occurs at plus and minus 50 Oe representing the field where the acoustic wave is driving magnetic oscillations.

1.5 Dissertation Overview

In this dissertation, magnetic and acoustic devices are explored for the advancement of communication capabilities. Specifically, a strain powered antenna based on the interactions between piezoelectricity and magnetostriction (i.e. multiferroic effect) is examined in Chapter 2. The design of the antenna is motivated by the challenge of communicating in RF denied media such as seawater. Thus, a low frequency magnetic antenna based on strain is considered. In Chapter 3 nonlinear Lamb wave devices that act as a frequency mixer and filter in a single component are experimentally demonstrated. Additionally, a circuit model is developed that closely matches the experimental results and a analytical model is used to predict optimal device performance and size. Lastly, in Chapter 4 strain tuned magnetic filters are explored. These filters utilize strain to control the permeability of dipole coupled ellipses. Tunable filters such as the ones explored in this dissertation have a wide variety of applications such as in the front end of radios employing spectrum sensing techniques such as cognitive radio and software defined radio.

1.6 Chapter References

[1] A. Zangwill, *Modern Electrodynamics* (Cambridge University Press, Cambridge, 2013).

[2] R. M. White and F. W. Voltmer, "DIRECT PIEZOELECTRIC COUPLING TO SURFACE ELASTIC WAVES", Applied Physics Letters **7**, 314 (1965).

[3] C. Campbell, *Surface Acoustic Wave Devices and Their Signal Processing Applications* (Academic Press, INC., San Diego, 1989), p. 484.

[4] S. Qin and Y. E. Wang, "Parametric conversion with distributedly modulated capacitors (DMC) for low-noise and non-reciprocal RF front-ends", IEEE MTT-S International Microwave Symposium Digest, 0 (2013).

[5] D. M. Pozar, *Microwave Engineering*, 4th (John Wiley & Sons, Inc., Hoboken, 2012).

[6] J. D. Schneider, J. P. Domann, M. K. Panduranga, S. Tiwari, P. Shirazi, Z. Yao, C. Sennott, D. Shahan, S. Selvin, G. McKnight, W. Wall, R. N. Candler, Y. E. Wang, and G. P. Carman, "Experimental demonstration and operating principles of a multiferroic antenna", Journal of Applied Physics **126**, 10.1063/1.5126047 (2019).

[7] J. P. Domann and G. P. Carman, "Strain powered antennas", Journal of Applied Physics **121**, 44905 (2017).

[8] Z. Yao, S. Tiwari, T. Lu, J. Rivera, K. Q. Luong, R. N. Candler, G. P. Carman, and Y. E. Wang, "Modeling of Multiple Dynamics in the Radiation of Bulk Acoustic Wave Antennas", IEEE Journal on Multiscale and Multiphysics Computational Techniques **5**, 7 (2020).

[9] T. Nan, H. Lin, Y. Gao, A. Matyushov, G. Yu, H. Chen, N. Sun, S. Wei, Z. Wang, M. Li, X. Wang, A. Belkessam, R. Guo, B. Chen, J. Zhou, Z. Qian, Y. Hui, M. Rinaldi, M. E. McConney, B. M. Howe, Z. Hu, J. G. Jones, G. J. Brown, and N. X. Sun, "Acoustically

actuated ultra-compact NEMS magnetoelectric antennas", Nature Communications **8**, 1 (2017).

[10] P. K. Nordeen, "High Frequency Dynamics of Magnetoelastic Composites and Their Application in Radio Frequency Sensors", PhD thesis (University of California, Los Angeles, 2016).

[11] M. N. Srinivas Prasad, R. U. Tok, and Y. E. Wang, "Magnetic Pendulum Arrays for ULF Transmission", in 2018 ieee antennas and propagation society international symposium and usnc/ursi national radio science meeting, apsursi 2018 - proceedings, August (2018), pp. 71–72.

[12] J. P. Domann, "On Magnetoelastodynamics", PhD thesis (University of California, Los Angeles, 2016).

[13] J. D. Maines and E. G. Paige, "Surface-Acoustic-Wave Devices for Signal Processing Applications", Proceedings of the IEEE **64**, 639 (1976).

[14] K.-y. Hashimoto and T. Kimura, "Tunable RF SAW / BAW Filters : What are Possible and What are Not ?", 8522.

[15] K. M. Lakin and J. S. Wang, "Acoustic bulk wave composite resonators", Applied Physics Letters **38**, 125 (1981).

[16] R. H. Olsson, K. Hattar, S. J. Homeijer, M. Wiwi, M. Eichenfield, D. W. Branch, M. S. Baker, J. Nguyen, B. Clark, T. Bauer, and T. A. Friedmann, "A high electromechanical coupling coefficient SH0 Lamb wave lithium niobate micromechanical resonator and a method for fabrication", Sensors and Actuators, A: Physical **209**, 183 (2014).

[17] T. Ikeda, *Fundamentals of Piezoelectricity*, Oxford science publications (Oxford University Press, 1996).

[18] A. K. Mal and S. J. Singh, *Deformation of Elastic Solids* (Prentice Hall, 1991).

[19] A. G. Gurevich and G. A. Melkov, *Magnetization Oscillations and Waves* (CRC Press Inc., 1996).

[20] J. Coey, *Magnetism and Magnetic Materials* (Cambridge University Press, 2009).

[21] B. D. Cullity and C. Graham, *Introduction to Magnetic Materials*, 2nd (Wiley, New York, 2009).

[22] C. Kittel, "On the theory of ferromagnetic resonance absorption", Physical Review **73**, 155 (1948).

[23] J. D. Adam and S. N. Stitzer, "Frequency Selective Limiters for High Dynamic Range Microwave Receivers", IEEE Transactions on Microwave Theory and Techniques **41**, 2227 (1993).

[24] R. Aigner, "Tunable Filters? Reality Check Foreseeable Trends in System Architecture for Tunable RF Filters", IEEE Microwave Magazine **16**, 82 (2015).

[25] S. Gevorgian, A. Tagantsev, and A. K. Vorobiev, *Tuneable Film Bulk Acoustic Wave Resonators*, edited by B. Derby (Springer-Verlag London, 2013).

[26] A. C. Chavez, J. D. Schneider, A. Barra, S. Tiwari, R. N. Candler, and G. P. Carman, "Voltage-Controlled Ferromagnetic Resonance of Dipole-Coupled CoFeB Nanoellipses", Physical Review Applied **12**, 44071 (2019).

[27] J. P. Joule, "XVII. On the effects of magnetism upon the dimensions of iron and steel bars", The London, Edinburgh, and Dublin Philosophical Magazine and Journal of Science **30**, 76 (1847).

[28] Z. Yao, Y. E. Wang, S. Keller, G. P. Carman, S. S. Member, Y. E. Wang, S. S. Member, S. Keller, and G. P. Carman, "Bulk Acoustic Wave-Mediated Multiferroic Antennas: Architecture and Performance Bound", IEEE Transactions on Antennas and Propagation **63**, 3335 (2015).

[29] J. Xu, C. M. Leung, X. Zhuang, J. Li, S. Bhardwaj, J. Volakis, and D. Viehland, "A low frequency mechanical transmitter based on magnetoelectric heterostructures operated at their resonance frequency", Sensors (Switzerland) **19**, 10.3390/s19040853 (2019).

[30] A. A. Kundu, A. C. Chavez, S. M. Keller, G. P. Carman, and C. S. Lynch, "360° deterministic magnetization rotation in a three-ellipse magnetoelectric heterostructure", Journal of Applied Physics **123**, 104105 (2018).

[31] Y. C. Hsiao, R. Khojah, X. Li, A. Kundu, C. Chen, D. B. Gopman, A. C. Chavez, T. Lee, Z. Xiao, A. E. Sepulveda, R. N. Candler, G. P. Carman, D. Di Carlo, and C. S. Lynch, "Capturing magnetic bead-based arrays using perpendicular magnetic anisotropy", Applied Physics Letters **115**, 10.1063/1.5085354 (2019).

[32] Z. Xiao, R. Lo Conte, C. Chen, C.-Y. Liang, A. Sepulveda, J. Bokor, G. P. Carman, and R. N. Candler, "Bi-directional coupling in strain-mediated multiferroic heterostructures with magnetic domains and domain wall motion", Scientific Reports **8**, 5207 (2018).

[33] Z. Xiao, K. P. Mohanchandra, R. Lo Conte, C. Ty Karaba, J. D. Schneider, A. Chavez, S. Tiwari, H. Sohn, M. E. Nowakowski, A. Scholl, S. H. Tolbert, J. Bokor, G. P. Carman, and R. N. Candler, "Enhanced magnetoelectric coupling in a composite multiferroic system via interposing a thin film polymer", AIP Advances **8**, 55907 (2018).

[34] A. A. Kundu, "Multiferroics for Future Cell Sorting Devices", PhD thesis (University of California Los Angeles, 2019).

[35] J. D. Schneider, Q. Wang, Y. Li, A. C. Chavez, J.-Z. Hu, and G. Carman, "RF voltage-controlled magnetization switching in a nano-disk", Journal of Applied Physics **126**, 163903 (2019).

[36] A. Barra, J. Domann, K. W. Kim, and G. Carman, "Voltage Control of Antiferromagnetic Phases at Near-Terahertz Frequencies", Physical Review Applied **9**, 34017 (2018).

[37] Q. Wang, J. Z. Hu, C. Y. Liang, A. Sepulveda, and G. Carman, "Voltage-induced strain clocking of nanomagnets with perpendicular magnetic anisotropies", Scientific Reports **9**, 1 (2019).

[38] Q. Wang, "Voltage Control of Perpendicular Magnetization in Multiferroics", PhD thesis (University of California, Los Angeles, 2018).

[39] Q. Wang, X. Li, C.-Y. Y. Liang, A. Barra, J. Domann, C. Lynch, A. Sepulveda, and G. Carman, "Strain-mediated 180° switching in CoFeB and Terfenol-D nanodots with perpendicular magnetic anisotropy", Applied Physics Letters **110**, 102903 (2017).

[40] C.-Y. Y. Liang, S. M. Keller, A. E. Sepulveda, A. Bur, W.-Y. Y. Sun, K. Wetzlar, and G. P. Carman, "Modeling of magnetoelastic nanostructures with a fully coupled mechanical-micromagnetic model", Nanotechnology **25**, 435701 (2014).

[41] A. C. Chavez, A. Barra, and G. P. Carman, "Voltage control of magnetic monopoles in artificial spin ice", Journal of Physics D: Applied Physics **51**, 10.1088/1361-6463/aac0ae (2018).

[42] A. C. Chavez, "Voltage Control of Magnetism in Nanoscale Artificial Multiferroics", PhD thesis (University of California, Los Angeles, 2018).

[43] A. Barra, "Magnetic Memory with Antiferromagnets and Multilayers", PhD thesis (University of California, Los Angeles, 2019).

[44] J. P. Domann, C. M. Loeffler, B. E. Martin, and G. P. Carman, "High strain-rate magnetoelasticity in Galfenol", Journal of Applied Physics **118**, 10.1063/1.4930891 (2015).

[45] D. Labanowski, A. Jung, and S. Salahuddin, "Power absorption in acoustically driven ferromagnetic resonance", Applied Physics Letters **108**, 22905 (2016).

[46] D. Labanowski, V. P. Bhallamudi, Q. Guo, C. M. Purser, B. A. McCullian, P. Chris Hammel, and S. Salahuddin, "Voltage-driven, local, and efficient excitation of nitrogen-vacancy centers in diamond", Science Advances **4**, eaat6574 (2018).

[47] X. Li, D. Labanowski, S. Salahuddin, and C. S. Lynch, "Spin wave generation by surface acoustic waves", Journal of Applied Physics **122**, 43904 (2017).

[48] P. Kuszewski, I. S. Camara, N. Biarrotte, L. Becerra, J. Von Bardeleben, W. Savero Torres, A. Lemaître, C. Gourdon, J. Y. Duquesne, and L. Thevenard, "Resonant magneto-Acoustic switching: Influence of Rayleigh wave frequency and wavevector", Journal of Physics Condensed Matter **30**, 10.1088/1361-648X/aac152 (2018).

[49] K. Nygren, J. Schneider, Q. Wang, D. Labanowski, S. Salahuddin, G. Carman, and K. Buchanan, "On and Off-Resonance Spin Wave/Surface Acoustic Wave Coupling Measured Using Brillouin Light Scattering", in Aps march meeting abstracts, Vol. 2019, APS Meeting Abstracts (Jan. 2019), p. C41.011.

[50] S. Chikazumi, *Physics of Ferromagnetism*, Vol. 1, International Series of Monographs on Physics 11 (Oxford University Press, Oxford, 1997), p. 655.

2 Underwater Antennas

2.1 Introduction

Communicating underwater [1], through the ground [2], and inside the body [3] requires antennas capable of transmitting signals in lossy electrically conductive environments (e.g. sea water) [1, 4, 5]. For these applications, ultra-low frequencies (ULF) (300 Hz to 3 kHz) are often utilized due to the increased signal penetration depth, or skin depth, at these frequencies [4, 6–8]. However, the large electromagnetic (EM) wavelength (e.g. 100 km at 3 kHz) makes portability challenging for conventional electric antennas that rely on an electromagnetic resonance for efficient operation. Recent research is now focusing on near field communication with electrically small magnetic antennas to overcome some of these obstacles [9]. Magnetic antennas differ from their electric counterparts in that the region close to the antenna (i.e. the near field) is predominantly comprised of magnetic fields rather than electric fields. As a result, they exhibit substantially smaller near-field losses and propagate signals to larger distances with losses up to three orders of magnitude smaller in lossy electrically conductive environments [9]. While standard loop antennas can be used here, they generate low magnetic moments and therefore low signal strengths. New methods for creating electrically small magnetic antennas with large signal strengths are needed to advance their use in lossy environments.

Magnetic antennas utilizing mechanical manipulation have recently been explored to achieve these large signal strengths. One approach mechanically rotates permanent magnets to control large magnetic fields [10]. However, this approach requires the manipulation of large inertial forces that make signal modulation challenging and low bandwidth while also raising structural integrity concerns. Additionally, multiferroic composites consisting of layered piezoelectric and magnetostrictive [11–17] materials have been explored for magnetic antennas [18–22] [22–26]. These multiferroic antennas use voltage driven piezoelectric strains to directly manipulate magnetic spin states in the magnetostrictive material [18] as contrasted with rotating

permanent magnets (i.e. eliminates inertial forces). Analytical and numerical models have shown that these multiferroic antennas [18, 21] exploit the slower acoustic waves rather than relying solely on the faster EM wave speeds to reduce antenna size and increase relative performance (i.e., they rely on exciting a mechanical resonance). This allows for a multiferroic antenna much smaller than the electromagnetic wavelength (i.e. an electrically small antenna) to resonate without requiring additional bulky capacitors and inductors to tune an electromagnetic resonance and also avoids the ohmic losses associated with those components. However, experimental validation of multiferroic antennas has been challenging due to low signal levels and contribution from radiating elements other than the magnetostrictive material [19, 23]. While both the multiferroic models and experiments are promising, more detailed measurements and comparisons are needed to both validate and understand the new electrically small multiferroic antennas.

In this work, a multiferroic near field antenna is experimentally demonstrated. The system consists of a piezoelectric PZT-5H stack mechanically in series with an iron gallium (FeGa) magnetostrictive rod. The experiments consist of applying a voltage to the PZT, measuring the dynamic stress, strain, magnetic field, and magnetic flux in the FeGa, while also measuring the magnetic field in free space. These tests are conducted as a function of bias magnetic field and PZT voltage amplitude. The experimental data are compared with an analytical dipole model providing good agreement and eliminating the concern over noise and interference contributions. Finally, we suggest an optimal FeGa aspect ratio to maximize control of the magnetic energy modulated in free space around the antenna.

2.2 Analysis

In this section two types of antennas are analytically compared, one with a magnetic current source and one with an electric current source. The analysis is based on a auxiliary vector potential approach where point sources are assumed. The goal of this section is to get a better

understanding of when a magnetic current source is more beneficial than an electric current source. Thus, the surrounding media is taken into consideration. Additionally, higher order terms are not neglected in the analyses and thus far-field radiation is not assumed but handled automatically when the fields are analyzed far from the source. The metric for comparison will be the radiated (real) power from electrically small ($\lambda/100$) sources normalized to the input power.

The electric field and magnetic fields generated from a magnetic current source or an electric current source can be found by first solving for their respective vector potentials [8]. Specifically, the magnetic vector potential $\vec{A}$ for an electric current source and the electric vector potential $\vec{F}$ for a magnetic current source given below in Equations 2.1 and 2.2 respectively

$$\vec{A} = \frac{\mu}{4\pi}\int_{\Omega} \vec{J}\frac{e^{-(\alpha+j\beta)R}}{R}d\Omega' \tag{2.1}$$

and

$$\vec{F} = \frac{\varepsilon}{4\pi}\int_{\Omega} \vec{M}\frac{e^{-(\alpha+j\beta)R}}{R}d\Omega' \tag{2.2}$$

where μ is the permeability, ε is the permittivity, R is the distance from the source to the observation point ($R = r - r'$), α is the attenuation constant, β is the phase constant, and $\vec{J}$ and $\vec{M}$ are electric and magnetic current densities respectively. The attenuation and phase constant are functions of the surrounding media's material properties (i.e. conductivity (σ), ε, and μ) and the operating frequency of the antenna (ω). Thus α and β are given as [8]

$$\alpha = \omega\sqrt{\mu\varepsilon}\left(\frac{1}{2}\left[\sqrt{1+\frac{\sigma}{\omega\varepsilon}^2}-1\right]\right)^{1/2} \tag{2.3}$$

and

$$\beta = \omega\sqrt{\mu\varepsilon}\left(\frac{1}{2}\left[\sqrt{1+\frac{\sigma}{\omega\varepsilon}^2}+1\right]\right)^{1/2} \tag{2.4}$$

For linear electric and magnetic currents Equations 2.1 and 2.2 reduce to

$$\vec{A} = \frac{\mu}{4\pi}\int_{-l/2}^{l/2} \vec{I}_e\frac{e^{-(\alpha+j\beta)R}}{R}dl' \tag{2.5}$$

and

$$\vec{F} = \frac{\varepsilon}{4\pi}\int_{-l/2}^{l/2}\vec{I}_m\frac{e^{-(\alpha+j\beta)R}}{R}dl' \tag{2.6}$$

where $\vec{I}_e$ and $\vec{I}_e$ are electric and magnetic currents respectively. Assuming the source is located at the origin, orientated along the z-axis, and $l << \lambda$, $\vec{A}$ and $vecF$ further reduced to

$$\vec{A} = \frac{\mu}{4\pi}j\omega PV\frac{e^{-(\alpha+j\beta)r}}{r}\hat{z} \tag{2.7}$$

and

$$\vec{F} = \frac{\varepsilon}{4\pi}j\omega BV\frac{e^{-(\alpha+j\beta)r}}{r}\hat{z} \tag{2.8}$$

where P and B are the amplitude of electric polarization density and flux density changes respectively and V is the volume of the source. Once the vector potentials are known, the electric ($\vec{E}$) and magnetic ($\vec{H}$) fields are calculated using

$$\vec{H}_A = \frac{1}{\mu}\nabla\times\vec{A} \tag{2.9}$$

and

$$\vec{E}_A = -j\omega\vec{A} - \frac{j}{\omega\varepsilon\mu}\nabla\left(\nabla\cdot\vec{A}\right) \tag{2.10}$$

for the $\vec{A}$ vector potential. While $\vec{H}$ and $\vec{E}$ from the $\vec{F}$ vector potential are calculated using

$$\vec{E}_F = -\frac{1}{\varepsilon}\nabla\times\vec{F} \tag{2.11}$$

and

$$\vec{H}_F = -j\omega\vec{F} - \frac{j}{\omega\varepsilon\mu}\nabla\left(\nabla\cdot\vec{F}\right) \tag{2.12}$$

respectively. From the electric and magnetic fields, the time-average power density (Poynting vector) can be determined using

$$\vec{P} = \frac{1}{2}\vec{E}\times\vec{H}^* \tag{2.13}$$

To determine the total power, Equation 2.13 is integrated over the surface of a sphere. The real part is the radiated power and the imaginary part is the reactive power. For the remainder of the

analysis, the focus will be the radiated power.

To compare the performance between the magnetic dipole and the electric dipole, the radiated power is normalized to the input power for each respective source. The input power is determined by considering the total power loss in the media surrounding the antenna given by

$$P_{loss} = \int_0^{2\pi} \int_0^{\pi} \int_a^{\infty} \frac{1}{2} \vec{E} \cdot \vec{E}^* r^2 \sin(\theta) dr d\theta d\phi \tag{2.14}$$

where a is the radius of the smallest sphere enclosing the antenna. The integral in Equation 2.14 is taken over all space to represent the input power of each source because all of the power must be absorbed by the conductive media. This is similar to the analysis done in [9]. Thus, the metric for comparison for an electric source is given by

$$\mathrm{P}_{\mathrm{norm}}^{\mathrm{elec}} = \frac{\mathrm{P}_{\mathrm{rad}}^{\mathrm{elec}}}{\mathrm{P}_{\mathrm{loss}}^{\mathrm{elec}}} \tag{2.15}$$

and for a magnetic source is given by

$$\mathrm{P}_{\mathrm{norm}}^{\mathrm{mag}} = \frac{\mathrm{P}_{\mathrm{rad}}^{\mathrm{mag}}}{\mathrm{P}_{\mathrm{loss}}^{\mathrm{mag}}} \tag{2.16}$$

In addition to analyzing the power and field components of a magnetic antenna, consideration of the magnetic field energy stored in free space provides insight into how the antenna geometry and material properties impact overall performance. The amount of energy stored in free space around a magnetized material is given by [24]

$$U_{air} = \frac{1}{2} \mu_0 M^2 N (1 - N) \tag{2.17}$$

where N is the FeGa rod's magnetometric demagnetization factor and M is the magnetization. For small changes in strain or applied field, magnetization changes are approximately piezomagnetic, with $M = q^{eff}\varepsilon + \chi^{eff} H^a$ in 1 dimension. Here ε is the FeGa strain and H^a is the applied bias magnetic field. The effective piezomagnetic coefficient q^{eff} and effective susceptibility χ^{eff} are functions of the shape and are defined as $q^{eff} = \frac{1}{(1+N\chi)}$ and $\chi^{eff} = \frac{1}{(1+N\chi)}$, where

q and χ are the piezomagnetic coupling coefficient and susceptibility respectively. Substituting M into Equation 2.17 and taking the derivative with respect to strain yields the strain-energy coupling in free space.

$$\alpha = \frac{\partial U_{air}}{\partial \varepsilon} = \frac{q\mu_0 \left(N - N^2\right)\left(q\varepsilon + \chi H^a\right)}{\left(1 + N\chi\right)^2} \tag{2.18}$$

Equation 2.18 indicates how easily the free space energy can be modulated with strain. It has a non-linear dependence on the antenna geometry through the demagnetization factor N. Taking the derivative of Equation 2.18 with respect to N and setting it equal to zero yields a relationship for determining the demagnetizing factor allows the largest energy modulation with respect to applied strain

$$N_{opt} = \frac{1}{2 + \chi} \tag{2.19}$$

A cylinder's longitudinal demagnetizing factor is $N_{cy} = AR^{-1}\left(AR + 1 - AR\sqrt{1 + AR^{-2}}\right)$ [25], where AR=L/r is the aspect ratio (i.e. ratio of the length to the radius) of the cylinder. Substituting N_{cy} into Equation 2.19 provides a relationship for determining the AR that maximizes strain-mediated control over the free space energy.

2.3 Experimental Setup

The multiferroic near field antenna shown in Figure 2.1 operates through stress induced magnetization changes in a magnetoelastic rod. In this setup, a sinusoidal voltage applied to a piezoelectric (PZT) stack produced dynamic axial compressive stresses in an $Fe_{80.77}Ga_{19.23}$ (FeGa) rod, where the composition of the FeGa was verified using inductively coupled plasma mass spectrometry. Consequently, the magnetization creates changes in the magnetic near field to transmit information. As seen in the figure, the antenna consisted of two 50 mm long PZT piezoelectric stack actuators (75 μm thick layers) mechanically in series with an 80 mm long 4 mm diameter FeGa rod. The PZT was mechanically fixed at one end while the FeGa rod was mechanically fixed at the other end within an ULTEM 1000 Natural PEI housing (2.1 1b). Titanium spacers between the PZT and FeGa were used to uniformly distribute the applied

load. A constant bias field was applied by placing the near field antenna inside a solenoid. The solenoid extended 25 mm past the ends of the FeGa rod, placing the magnetic material in a uniform applied magnetic field. Briefly, we note that designs more efficiently stressing the magnetic material are possible (e.g., resonant bending setups) which would result in a different magnetic response. This setup provides a flexible proof-of-concept testbed to characterize the antenna and material.

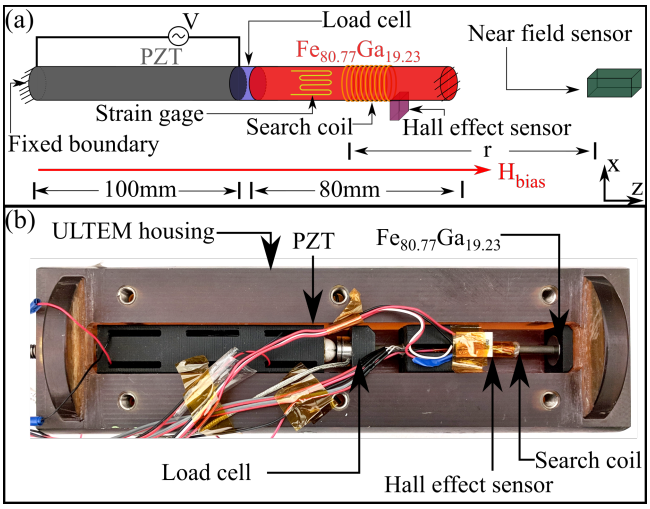

Figure 2.1: (a) Schematic of the experimental setup for the multiferroic near field transmitter. (B) Photograph of the experimental setup.

The multiferroic near field antenna's mechanical and magnetic responses were measured with several sensors placed on and near the antenna. The FeGa dynamic mechanical response was measured with a 1kN load cell (accuracy of ±7.5 N RMS) and two 120 Ohm strain gages placed halfway along the rod's length on opposite sides (i.e., circumferentially spaced 180 degrees apart). The magnetic field (H_{bias}) was measured with a hall effect sensor placed adjacent to the FeGa rod. The FeGa flux density (B_{mat}) was measured with a 100 turn search coil using 25 gage wire connected to a fluxmeter with a resolution of 1 μT. The magnetic near field (B_{air}) was monitored with a fluxgate magnetometer having a noise floor of $< 10\frac{pTrms}{\sqrt{Hz}}$. Data was digitally collected with a 2 kHz sampling rate.

Tests were conducted to measure the near field magnetic response as a function of bias magnetic field and PZT voltage. Initial testing was used to determine the unstressed material magnetically saturated at an applied field of 16 kA/m. For this study, the magnetic bias field

was swept from 0 to 23 kA/m in 21 steps. At each magnetic bias field, a sinusoidal voltage with peak voltages (Vp) of 20 V, 40 V, or 60 V was applied to the PZT stack at 10 Hz (i.e. $V = V_p/2 + V_p/2[\sin(2\pi(10)t)]$) resulting in highly localized electric fields between the parallel plates. Additionally, 200 cycles were recorded for each driving voltage and field combination to minimize noise for subsequent data analysis. The fluxgate magnetometer was positioned from 24 cm to 134 cm from the center of the FeGa rod in 10 cm steps along the FeGa axis as shown in Figure 2.1. A low pass Butterworth filter was used to remove the high frequency noise and a Fast-Fourier Transform provided the frequency response for each signal. The signals from the load cell, fluxgate magnetometer, and pickup coil have been temporally shifted to compensate for the phase shift introduced by each sensor's electronics.

In order to ensure B_{air} is due to B_{mat}, and not due to noise/interference, an analytical model was used to predict the near field response. The model assumes the multiferroic near field transmitter can be approximated as a dynamically changing magnetic dipole oriented along the +z direction (i.e. see analysis in Section 2.2). From Equation 2.12 the radial component of the dipole's magnetic field in spherical coordinates is

$$|\mathbf{B}_r| = \frac{\Delta B_{mat} V}{2\pi r^3} \sqrt{(1 + r^2\beta^2)\cos^2\theta} \tag{2.20}$$

where ΔB_{mat} is the measured FeGa flux density from the search coil, V is the FeGa volume, r is distance (see Figure 2.1), μ_0 is the permeability of free space, β is the free space wave number, and θ is the polar angle. The search coil flux density was assumed uniform throughout the FeGa rod.

2.4 Results

Figure 2.2 plots analytical calculations of the ratio P_{norm}^{mag} (Equation 2.16) to P_{norm}^{elec} (Equation 2.15) in dB as a function of antenna size (i.e. radius of the smallest sphere enclosing the

antenna). For this calculation it is assumed that the observation point (r) is 1 km from the source, additionally, three frequencies are considered 1 kHz (blue line), 5 kHz (orange line), and 10 kHz (green line). It is also assumed that the antenna is fully submerged in seawater with conductivity $\sigma = 5$ S/m and relative permittivity $\varepsilon_r = 70$ [26]. Each of the lines in Figure 2.2 show the same trend, the smaller the antenna the more beneficial it is to have a magnetic source as opposed to an electric source. Specifically, focusing on the blue 1 kHz line, the magnetic source is approximately 32 dB better when a is 15 cm. When a is increased to 60 cm the magnetic source still out performs the electric source by 18 dB. The reason the magnetic source is a better option is because the electric field for a magnetic source is proportional to $1/r^2$ while for an electric source the electric field is proportional to $1/r^3$. Thus, in the near field, there is more Ohmic losses associated with the electric source [9, 10, 14, 26] . This plot shows that communicating in conductive RF-denied media, a magnetic source outperforms an electric source.

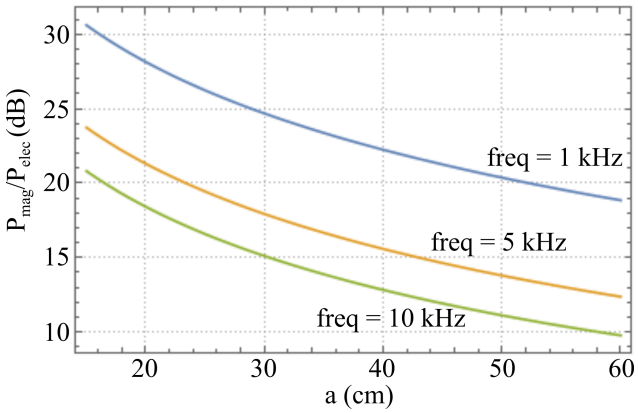

Figure 2.2: Analytical calculations comparing the power radiated from a magnetic source and an electric source when both sources are fully submerged in seawater at a distance of 1 km.

Figure 2.3 plots the measured data for the multiferroic near field antenna as a funtion of time. Figure 2.3a and 2.3b, show the stress (σ) and flux density in the FeGa rod (B_{mat}) respectively, and Figure 2.3c shows the magnetic ear field (B_{air}) measured 20 cm from the end of the FeGa rod (24 cm from the middle). The driving electric and constant magnetic fields were 0.4 MV/m and 4 kA/m, respectively. The amplitudes of each signal are labeled as $\Delta\sigma$, ΔB_{mat}, and ΔB_{air} respectively. As can be seen in Figure 2.3(a-c), the changes in stress, magnetic flux, and the free-space magnetic field are al sinusoidal outputs as the PZT is electricall actuated. The lack

of additional harmonics in these signals indicates the applied stress is low enough that the magnetoelastic FeGa layer can accurately be approximated as piezomagnetic (i.e., linear) in the subsequent analysis. The additional low frequency variation in the B_{air} signal is attributed to drift in the sensor.

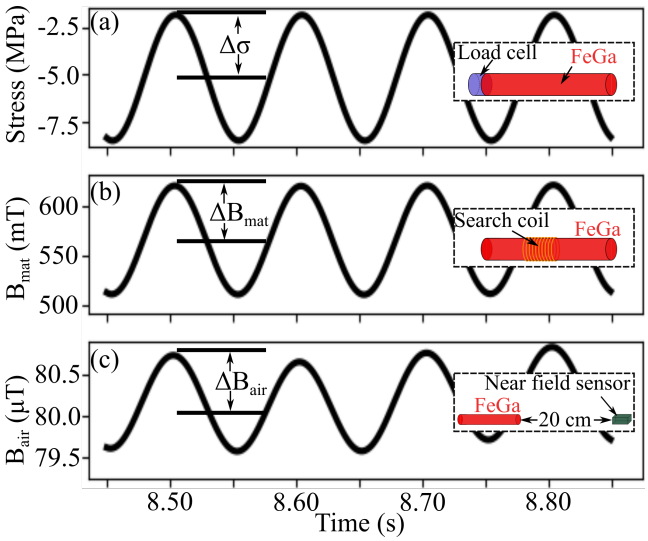

Figure 2.3: (a) Time response of the multiferroic near field antenna. (a) is the stress, (b) is the change in magnetization in the FeGa rod, and (c) is the near field sensor at 20 cm.

Figure 2.4 plots experimental data for ΔB_{mat} as a function of H_{bias} for AC electric field amplitudes of 0.13, 0.27, and 0.4 MV/m applied to the PZT. The schematics in the figures are used to illustrate the magnetic domain configuration before and after the application of stress at three H_{bias} points, 0 kA/m, 4 kA/m, and 23 kA/m. Focusing on the 0.27 MV/m electric field curve, there is an initial absence of ΔB_{mat} at $H_{bias} = 0$ kA/m followed by increasing ΔB_{mat} until a peak occurs at $H_{bias} = 4$ kA/m. Further H_{bias} increases produces a decreasing ΔB_{mat} until ΔB_{mat} 0 for large H_{bias}. This can be explained as follows. Initially, at $H_{bias} = 0$, the sample starts with zero net magnetization and when strain is applied the magnetic domains locally change, but on average vectorially cancel. As H_{bias} increases, the domains with magnetization parallel to H_{bias} become larger resulting in a net magnetization, allowing strain induced changes in B_{mat}. At the peak response ($H_{bias} = 4$ kA/m), the effective magnetoelastic field introduced by the stress is approximately equal and opposite to the applied magnetic field (i.e. external field) resulting in maximum change in ΔB_{mat}. As H_{bias} increases further, the strain energy becomes small compared to the Zeeman energy, and no longer capable of driving large changes. Similar trends

are present in both the 0.40 MV/m and the 0.13 MV/m curves. Additionally, both ΔB_{mat} and the optimal H_{bias} increase with increasing electric field strength. This trend is also reported in [27]. The shift in optimal H_{bias} is attributed to the effective magnetoelastic field being sufficiently large to reduce the flux density in a more magnetically ordered system at higher H_{bias}. Note that there are statistical modeling methods available to quantitatively describe the material responses discussed above [28].

Figure 2.4 inset provides experimentally measured stress-strain curves for the 0.27 MV/m oscillating electric field at three different H_{bias}. Each H_{bias} location is circled on the 0.27 MV/m curve. For H_{bias} = 0 kA/m the loss tangent (tanδ), calculated from the complex elastic modulus, is 0.122. This relatively large tanδ is caused by mechanically driven magnetic domain wall motion, even though the net change in magnetization is negligible ΔB_{mat} 0. At H_{bias} = 4 kA/m, the tanδ decreases to 0.042 due to reduced domain wall motion even though this mechanical loading produces large ΔB_{mat} in the FeGa rod. For H_{bias} = 23 kA/m the tanδ is very small (0.009) producing a nearly linear elastic response. This indicates the applied magnetic field Zeeman energy effectively pins the magnetization states and the applied load is insufficient to cause magnetization changes. It is worth highlighting that as H_{bias} increases from 0 kA/m to 4 kA/m the hysteresis decreases almost 3x even though the net ΔB_{mat} substantially increases through that same interval. This is largely due to a shift from completely incoherent motion of numerous domain walls at 0 field, to the motion of fewer walls and partial domain rotation at higher field strengths.

Figure 2.5 plots experimental data for the field in free-space ΔB_{air} 134 cm from the FeGa rod's center as a function of H_{bias} for the same three oscillating electric fields shown in Figure 2.4. When H_{bias} = 0, all three ΔB_{air} values are zero. This should be expected because ΔB_{mat} 0 in the FeGa rod at this bias field (Figure 2.4). As H_{bias} increases, the ΔB_{air} values increase and reach peak values of 1.34, 3.46, and 6.05 nT for electric fields of 0.13, 0.27, 0.40 MV/m respectively. The ΔB_{air} values increase by 139% and 342% as the electric field is increased. Similar ΔB_{mat} increases of 149% and 362% were measured in Figure 2.4. Therefore, to a large

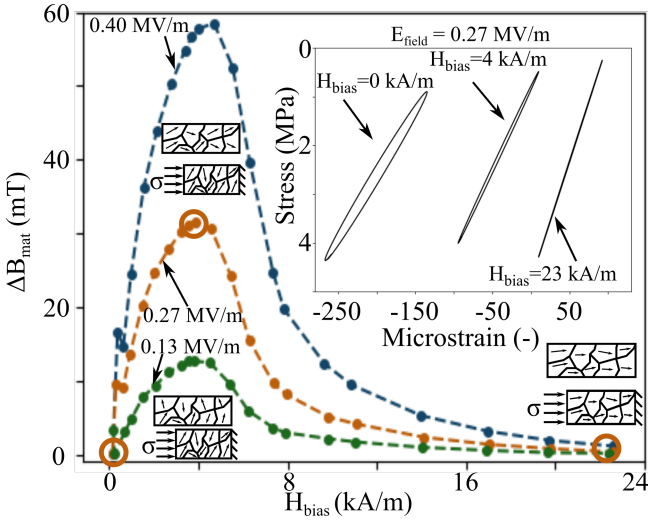

Figure 2.4: Amplitude of the change in magnetization in the FeGa rod as a function of magnetic field for 3 different oscillating electric fields to the PZT. The inset shows stress strain curves at three different magnetic fields for the 0.27 MV/m driving electric field.

extent $\Delta B_{air} \propto \Delta B_{mat}$. Additionally, the peak values occur at a higher H_{bias} for larger driving electric fields for reasons similar to those explained for Figure 2.4. As H_{bias} increases beyond the peaks, ΔB_{air} decreases in a similar fashion presented in Figure 2.4. The similarity of the curve shapes in Figures 2.4 and 2.5 coupled with the relative changes in the measurements of ΔB_{air} and ΔB_{mat} at different electric field amplitudes provides ample support that ΔB_{air} is caused by stress induced changes in the FeGa rod magnetization (i.e. the magnetoelastic effect).

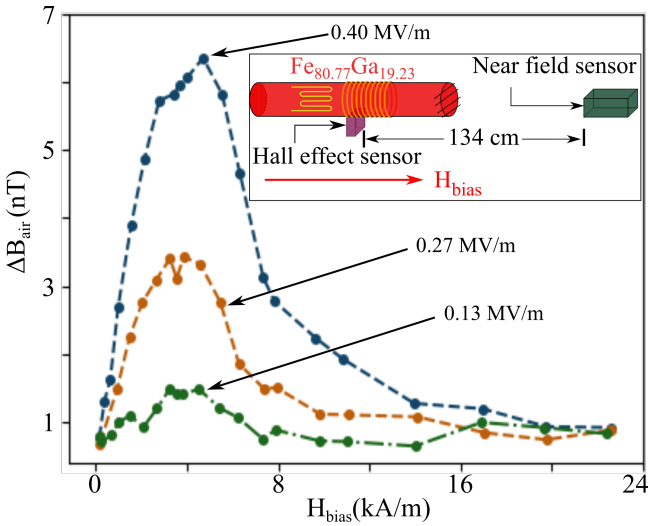

Figure 2.5: Amplitude of the near field sensor when placed 130 cm from the FeGa rod as a function of magnetic field.

Figure 2.6 compares the experimentally measured ΔB_{air} with an analytical magnetic dipole model (i.e. Equation 2.20) as a function of distance from the center the FeGa rod (see Figure 2.1a). This is presented for three driving electric fields with H_{bias} = 4 kA/m. The symbols represent measured data while the lines represent the analytical model. There is generally good agreement between the analytical model and experimental data as a function of distance for the three driving electric fields. Furthermore, the mean error for each of the driving electric fields is 25%. The discrepancy is attributed to the assumption that the FeGa rod can be represented by an infinitesimally small dipole in the analytical model rather than a more complex 3D magnetic structure that is actually present in the experiments. Regardless of this slight discrepancy, the agreement between the experiments and model demonstrates that the dynamic changes in air can be adequately represented with a magnetic dipole model presented in Equation 1. Furthermore, agreement is expected to improve as distance from the antenna increases and the higher order multipole moments become less important relative to the dipole field.

The inset of Figure 2.6 uses the analytical model (Equation 2.20) to determine the upper bound of ΔB_{air} normalized to the volume of the FeGa rod extrapolated to larger distances up to 1 km. This study is conducted to determine the volume of material needed to achieve a field strength of 1 fT at 1 km. This value represents a specified metric with large enough field strengths at the location of the receiver such that the signals are above ambient environmental noise and thus can be detected by a sensitive receiver. For these predictions three ΔB_{mat} are considered 1.0, 1.3, and 1.6 T with the largest representing the maximum possible change in FeGa [12]. The results demonstrate that 1 fT is achievable at 1 km distance with a 1.3 T change in flux density of the FeGa rod in volumes as small as 5 cm3, this equates to a magnetic moment change of 5.17 Am.

The multiferroic near field antenna setup is used to also track the cyclic energy flow from the input electric energy (U_{in}) to the change in magnetic energy in free space (ΔU_{air}). The input energy is calculated using $U_{in} = \frac{1}{2}CV_p^2$ where C is the piezoelectric capacitance and V_p is the peak applied voltage. For a 0.27 MV/m electric field and H_{bias} = 4 kA/m the input energy is

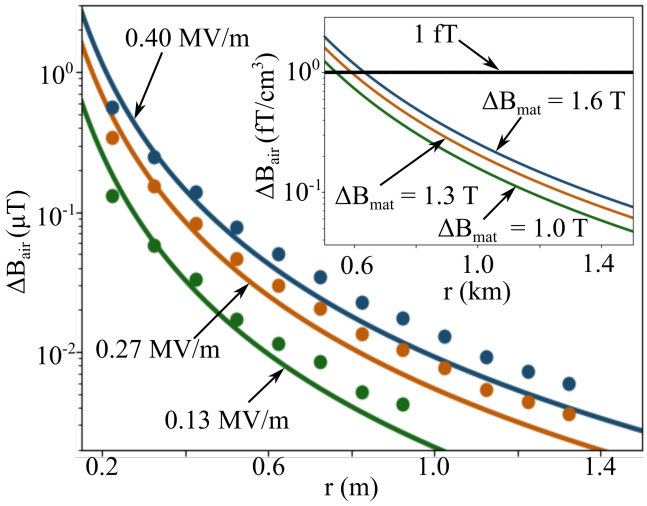

Figure 2.6: Comparison between measured near field data and the analytical model (i.e. equation 1) as a function of distance. The inset shows the predicted near field results out to 1.4 km.

calculated to be 27.2 mJ. The energy transferred to the FeGa rod calculated by integrating the stress strain curves is 0.24 mJ. The large energy decrease observed from input (27.2 mJ) to 0.24 mJ FeGa energy is due to stiffness matching issues between the FeGa and PZT [29], use of an axial loading method (i.e., instead of bending), as well as the test fixture's compliance. Increasing the energy transfer has been extensively studied by the smart materials community with accepted upper bounds on energy transfers of 1/4 achievable [29]. However, maximizing the energy transferred from the FeGa rod into free space (ΔU_{air}) has received far less attention. For this loading scenario, $\Delta U_{air} = 0.036$ mJ as calculated with Equation 2.17 (i.e. $M = \frac{\Delta B_{mat}}{\mu_0}$). However, Equation 2.17 suggests ΔU_{air} is a function of aspect ratio (AR) and the shape was not optimized for the experimental work.

Figure 2.7 uses Equations 2.18 and 2.17 to plot the normalized free-space coupling coefficient $\frac{\alpha}{\alpha_{max}}$ as a function of AR for FeGa susceptibilities χ of 60, 120, 180, and 240. The α values are normalized to the maximum α_{max} value of $\chi = 240$ (i.e. an approximate upper bound on χ [30]). For small aspect ratios (i.e. a disk) in Figure 2.7, the $\frac{\alpha}{\alpha_{max}}$ is trivially small because the demagnetizing effects increases the energy barrier for magnetization alignment along the axial direction. As AR increases, α increases reaching a maximum value labeled by AR_{opt}. Further increases in AR reduces $\frac{\alpha}{\alpha_{max}}$, this is because α is the product of $\frac{\partial U_{air}}{\partial M}$ and $\frac{\partial M}{\partial \varepsilon}$ and while increas-

ing AR increases the second term, it decreases the first term even faster due to it's dependance on the squared demagnetization factor. This results in higher changes of flux density but those changes have less of an effect on the free space energy. Therefore, the AR_{opt} represents a balance between the free space energy and applied strain to maximize magnetization rotation, i.e. maximize α.

Figure 2.7 inset plots $\frac{U_{air}}{U_{max}}$, normalized to max U_{air} at χ = 240, as a function of AR for the same four χ parameters. Here, similar trends are observed with the exception that $\frac{U_{air}}{U_{max}}$ has a stronger dependence on χ variations compared to $\frac{\alpha}{\alpha_{max}}$. The stronger dependence is caused by higher magnetization amplitudes for higher χ producing larger $\frac{U_{air}}{U_{max}}$ while $\frac{\alpha}{\alpha_{max}}$ changes are more closely connected to magnetization changes rather than magnetization amplitudes. An MH curve of the unstressed material yielded a peak susceptibility of χ = 180 . Considering the case for χ = 180 curve in the Figure 2.7 inset, the ΔU_{air} increases 68% when increasing from the AR of the tested sample AR_t = 40 to $AR_{opt} \approx 180$ while maintaining a constant volume. Furthermore, this indicates an potential increase of ΔB_{air} at 1 m from 7.4 nT to 20.3 nT for a driving electric field of 0.27 MV/m. This shows that the AR of the ferromagnetic transmitter strongly determines the amount of field modulated in free space and should represent an important consideration in a near field antenna design.

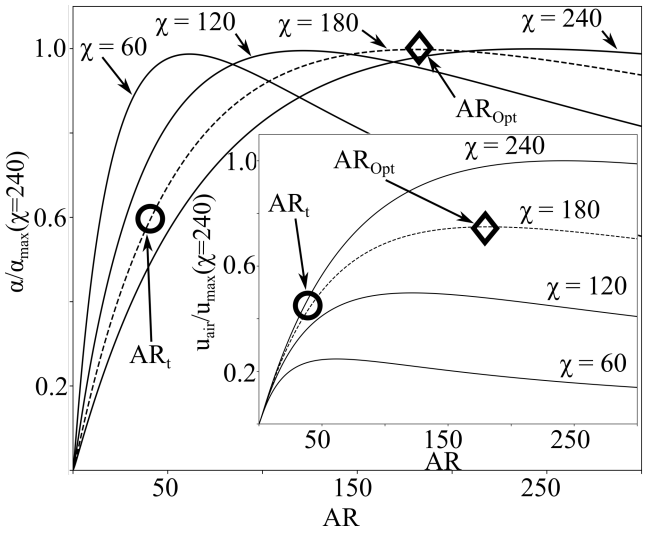

Figure 2.7: Strain-energy coupling as a function of AR (i.e. Equation 2.18) for four different χ. Inset plots the energy in free space as a function of AR (i.e. Equation 2.17) for four different χ.

2.5 Conclusion

A multiferroic antenna intended for communicating in the near field was demonstrated. The antenna used piezoelectric PZT-5H to apply a time varying stress to magnetoelastic iron gallium (FeGa) which produced magnetization changes in the FeGa. The magnetization changes showed dependence on voltage (stress) and magnetic bias field amplitude. The magnetic near field was measured and showed the same magnetic field dependence as the magnetization. Additionally, the measured magnetic near field was compared to an analytical model providing good agreement for 3 different amplitudes of applied stress. Furthermore, the analytical model showed that an appropriately designed multiferroic antenna can generate dynamic field levels of 1 fT at 1 km which is suitable for communicating underwater and through the ground. Lastly, the importance of using the proper geometry was highlighted by analyzing the flow of energy in the experimental setup. It was determined that an optimal aspect ratio can be found for a given FeGa susceptibility.

2.6 Chapter References

[1] I. F. Akyildiz, P. Wang, and Z. Sun, "Realizing underwater communication through magnetic induction", IEEE Communications Magazine **53**, 42 (2015).

[2] Z. Sun and I. F. Akyildiz, "Underground wireless communication using magnetic induction", IEEE International Conference on Communications, 1 (2009).

[3] P. Soontornpipit, C. M. Furse, and Y. C. Chung, "Design of implantable microstrip antenna for communication with medical implants", IEEE Transactions on Microwave Theory and Techniques **52**, 1944 (2004).

[4] D. F. Rivera and R. Bansal, "Towed antennas for US submarine communications: A historical perspective", IEEE Antennas and Propagation Magazine **46**, 23 (2004).

[5] T. Shaneyfelt, M. A. Joordens, K. Nagothu, and M. Jamshidi, "RF communication between surface and underwater robotic swarms", in 2008 world automation congress, wac 2008 (2008), pp. 1–6.

[6] D. M. Pozar, *Microwave Engineering*, 4th (John Wiley & Sons, Inc., Hoboken, 2012).

[7] M. A. Kemp, M. Franzi, A. Haase, E. Jongewaard, M. T. Whittaker, M. Kirkpatrick, and R. Sparr, "A high Q piezoelectric resonator as a portable VLF transmitter", Nature Communications **10**, 1 (2019).

[8] C. Balanis, *Advanced Engineering ElectroMagnetics*, 2nd (John Wiley & Sons, Inc., 2012).

[9] M. Manteghi and A. A. Y. Ibraheem, "On the study of the near-fields of electric and magnetic small antennas in lossy media", IEEE Transactions on Antennas and Propagation **62**, 6491 (2014).

[10] M. N. Srinivas Prasad, R. U. Tok, and Y. E. Wang, "Magnetic Pendulum Arrays for ULF Transmission", in 2018 ieee antennas and propagation society international symposium

and usnc/ursi national radio science meeting, apsursi 2018 - proceedings, August (2018), pp. 71–72.

[11] M. Wun-Fogle, J. B. Restorff, and A. E. Clark, "Soft and hard elastic moduli of Galfenol transduction elements (invited)", Journal of Applied Physics **105**, 10.1063/1.3058645 (2009).

[12] A. Mahadevan, P. G. Evans, and M. J. Dapino, "Dependence of magnetic susceptibility on stress in textured polycrystalline Fe81.6 Ga18.4 and Fe79.1 Ga20.9 Galfenol alloys", Applied Physics Letters **96**, 1 (2010).

[13] Z. Xiao, R. Lo Conte, C. Chen, C.-Y. Liang, A. Sepulveda, J. Bokor, G. P. Carman, and R. N. Candler, "Bi-directional coupling in strain-mediated multiferroic heterostructures with magnetic domains and domain wall motion", Scientific Reports **8**, 5207 (2018).

[14] J. D. Schneider, Q. Wang, Y. Li, A. C. Chavez, J.-Z. Hu, and G. Carman, "RF voltage-controlled magnetization switching in a nano-disk", Journal of Applied Physics **126**, 163903 (2019).

[15] A. C. Chavez, A. Barra, and G. P. Carman, "Voltage control of magnetic monopoles in artificial spin ice", Journal of Physics D: Applied Physics **51**, 10.1088/1361-6463/aac0ae (2018).

[16] Q. Wang, X. Li, C.-Y. Y. Liang, A. Barra, J. Domann, C. Lynch, A. Sepulveda, and G. Carman, "Strain-mediated 180° switching in CoFeB and Terfenol-D nanodots with perpendicular magnetic anisotropy", Applied Physics Letters **110**, 102903 (2017).

[17] Q. Wang, "Voltage Control of Perpendicular Magnetization in Multiferroics", PhD thesis (University of California, Los Angeles, 2018).

[18] Z. Yao, Y. E. Wang, S. Keller, G. P. Carman, S. S. Member, Y. E. Wang, S. S. Member, S. Keller, and G. P. Carman, "Bulk Acoustic Wave-Mediated Multiferroic Antennas:

Architecture and Performance Bound", IEEE Transactions on Antennas and Propagation **63**, 3335 (2015).

[19] T. Nan, H. Lin, Y. Gao, A. Matyushov, G. Yu, H. Chen, N. Sun, S. Wei, Z. Wang, M. Li, X. Wang, A. Belkessam, R. Guo, B. Chen, J. Zhou, Z. Qian, Y. Hui, M. Rinaldi, M. E. McConney, B. M. Howe, Z. Hu, J. G. Jones, G. J. Brown, and N. X. Sun, "Acoustically actuated ultra-compact NEMS magnetoelectric antennas", Nature Communications **8**, 1 (2017).

[20] J. Xu, C. M. Leung, X. Zhuang, J. Li, S. Bhardwaj, J. Volakis, and D. Viehland, "A low frequency mechanical transmitter based on magnetoelectric heterostructures operated at their resonance frequency", Sensors (Switzerland) **19**, 10.3390/s19040853 (2019).

[21] J. P. Domann and G. P. Carman, "Strain powered antennas", Journal of Applied Physics **121**, 44905 (2017).

[22] R. L. Kubena, X. Pang, K. G. Lee, Y. K. Yong, and W. S. Wall, "Wide-band multiferroic quartz MEMS antennae", in Journal of physics: conference series, Vol. 1407, 1 (2019), pp. 8–12.

[23] P. K. Nordeen, "High Frequency Dynamics of Magnetoelastic Composites and Their Application in Radio Frequency Sensors", PhD thesis (University of California, Los Angeles, 2016).

[24] J. Coey, *Magnetism and Magnetic Materials* (Cambridge University Press, 2009).

[25] H. A. Haus and J. R. Melcher, *Electromagnetic Fields and Energy* (Prentice Hall, 2017).

[26] R. Somaraju and J. Trumpf, "Frequency, Temperature and Salinity Variation of the Permittivity of Seawater", IEEE Transactions on Antennas and Propagation **54**, 3441 (2006).

[27] J. P. Domann, C. M. Loeffler, B. E. Martin, and G. P. Carman, "High strain-rate magnetoelasticity in Galfenol", Journal of Applied Physics **118**, 10.1063/1.4930891 (2015).

[28] P. G. Evans, M. J. Dapino, and J. B. Restorff, "Bill Armstrong memorial symposium: free energy model for magnetization and magnetostriction in stressed Galfenol alloys", Behavior and Mechanics of Multifunctional and Composite Materials 2007 **6526**, 652619 (2007).

[29] D. E. Heverly, K. W. Wang, and E. C. Smith, "Dual-Stack Piezoelectric Device with Bidirectional Actuation and Improved Performance", Journal of Intelligent Material Systems and Structures **15**, 565 (2004).

[30] R. A. Kellogg, A. B. Flatau, A. E. Clark, M. Wun-Fogle, and T. A. Lograsso, "Temperature and stress dependencies of the magnetic and magnetostrictive properties of Fe0.81Ga0.19", Journal of Applied Physics **91**, 7821 (2002).

3 Frequency Conversion Through Nonlinear Mixing in Lamb Waves

3.1 Introduction

Parametric coupling using a nonlinear circuit parameter (i.e. capacitance or inductance) to convert energy from one frequency to another was intensely studied in the 1950s [1, 2]. The parametric effect is used to create low noise microwave devices such as mixers, circulators, and parametric amplifiers [3–13]. One parametric coupling approach uses a transmission line periodically loaded with nonlinear capacitors to produce a time and space varying capacitance referred to as an electromagnetic (EM) Time Varying Transmission Line (TVTL) [8–10, 12, 13]. The EM-TVTL approach is a wide band technique covering a 0.5 to 2.5 GHz frequency range in millimeter sized devices. The relatively large EM wavelength at these frequencies make further size reduction challenging. One solution to reduce the TVTL's size is design structures with intrinsically slower wave speeds. One method uses acoustic waves with wave speeds five orders of magnitude smaller than EM waves. These acoustic devices rely on interdigitated transducers (IDTs), to create a variety of narrow band acoustic devices. Thus, a micron sized acoustic TVTL combining filters and mixers into a single component is possible. However, significant efforts investigating acoustic TVTLs have been inadequate.

The original EM-TVTL was inspired by analysis of a traveling-wave amplifier [1, 2, 14, 15] which consists of transmission lines coupled through a time-varying reactance. Recently, experimental results showed a EM-TVTL where the parametric coupling effect is induced through a transmission line periodically loaded with variable capacitors [9, 12, 13, 16]. The transmission line's nonlinear capacitance is modulated as a function of time and space at a frequency of f_c through a carrier wave. A signal at f_s traveling in the same direction as the carrier wave is inputted into the transmission line. The measured output signal consisted of three frequencies:

the original signal frequency, an up converted signal f_{c+s}, and a down converted signal f_{c-s}, where $f_{c+s} = f_c + f_s$ and $f_{c-s} = f_c - f_s$. The up and down converted frequencies are useful in a wide range of devices; however, device size reduction is challenging.

In contrast to the EM-TVTL acoustic waves have drastically slower wave speeds providing an opportunity to miniaturize the TVTL's physical dimensions [17–19]. The original concept was studied in the 1970s using a surface acoustic wave delay line with a third IDT placed between the input and output IDTs [20, 21][21]. In this original work, the third IDT is connected to an external circuit composed of nonlinear capacitors used to modulate the circuit conductance which is then electrically coupled to the acoustic wave through the IDT. However, this method still requires nonlinear capacitors, thus these device sizes are still relatively large. Another method to achieve acoustic parametric coupling uses a material with a nonlinear compliance [22]. In previous studies investigating the nonlinear compliance method, the chosen material was incapable of providing a large enough nonlinearity. However, most materials easily integrated into the acoustic design had insufficient nonlinearity to achieve the desired parametric coupling. Recently, researchers have reported that the compliance of aluminum nitride AlN varies an applied electric field [23] and strain [24, 25]. This suggests that AlN could be an ideal material to demonstrate a parametrically coupled acoustic device.

In this work, two different suspended Lamb wave devices [26] are designed, fabricated, and tested. Each device consists of three IDTs; 1) to launch a high-power strain wave, 2) to launch a low power signal wave, and 3) to receive an up converted or down converted wave. The high-power strain wave couples with the low power signal wave through the nonlinear compliance in the AlN. Experimental results show that a single device can be designed to simultaneously filter signals and down convert them or up convert them for further signal processing or transmission. Analytical modeling supports the experimental data and shows that acoustic TVTL devices can approach micron size dimensions.

3.2 Operating Principles and Fabrication

Figure 3.1 shows the design for the parametric Lamb wave device. The concept relies on two collinearly propagating Lamb waves in a suspended aluminum nitride (AlN) plate. The two waves are a high-power monochromatic Lamb wave (i.e. carrier wave) and a low-power Lamb wave (i.e. signal wave) at frequencies f_c and f_s respectively. The carrier wave induces a time and space varying compliance in the AlN resulting in the signal wave being mixed up and down in frequency with the carrier wave producing two additional frequency components (i.e. $f_m = f_c + f_s$ or $f_m = f_c - f_s$), this is termed parametric frequency conversion. To launch and receive the Lamb waves, three sets of interdigital transducers (IDTs) (composed of 34 fingers each) were used to convert electrical energy into acoustic energy and conversely acoustic energy into electrical energy through the piezoelectric effect [27, 28]. Shown in Figure 3.1(a), the left two sets of IDTs were responsible for launching the carrier (left IDT) and signal (middle IDT) waves and the right most IDT received the mixed wave at a frequency of f_m. The IDTs were each connected to ports labeled as P_3 (carrier), P_1 (signal), and P_2 (mixed).

Figure 3.1(b) shows a cross section of the Lamb wave device and Figure 3.1(c) shows a close-up schematic of the signal IDTs, where each finger pair is composed of a signal finger and a ground finger. The width and spacing between the individual fingers are equal to a quarter of an acoustic wavelength and are labeled as w_s. Thus, w_s was chosen based on the operating frequency and wave speed of the device. For these Lamb wave devices, the wave speed is approximately 8409 m/s. The fabrication process is shown in Figure 3.2 and is as follows: (1) starting with a blank (100) Si substrate with resistivity greater than 10 kΩ cm, 50 nm of platinum (Pt) was deposited and patterned; (2) 400 nm of AlN was deposited by reactive sputtering; (3) 100 nm of Al was deposited and patterned into IDTs; (4) release vents were etched into the AlN to provide access to the Si substrate; and (5) the Lamb wave devices were released by an isotropic etch of the Si under the AlN using XeF_2. Note, to release the devices using XeF_2, release vents must first be etched into the AlN using a reactive ion etch using BCl_3, Cl_2, and Ar. Figure 3.3 shows a scanning electron microscope image of a 550 μm thick AlN thin

film after etching. Ideally the side wall would be perfectly vertical, however, this is difficult to achieve because as the etching progresses more AlN is exposed causing the chamber to be loaded differently.

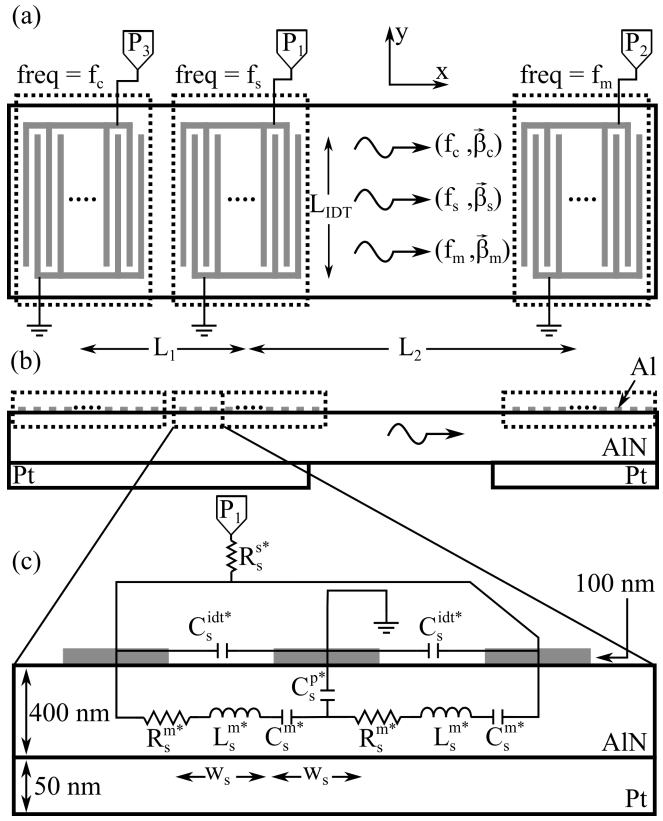

Figure 3.1: Design for the nonlinear Lamb wave device. (a) Top view of the design, (b) cross sectional view, (c) zoomed in schematic of the signal IDTs with an mBVD circuit model overlaying the device.

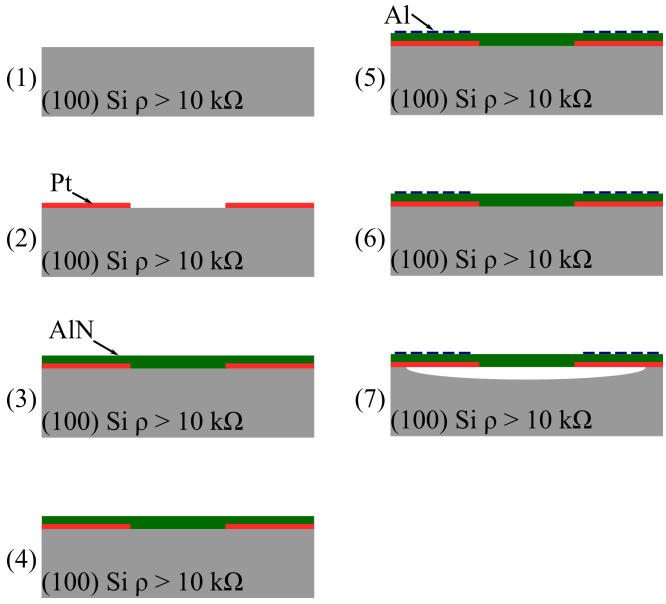

Figure 3.2: Fabrication diagram for the Lamb wave devices.

Figure 3.4 shows optical images of the fabricated Lamb wave devices. The top images show the completed devices before they were released in the XeF_2 etch, and the bottom images show a zoomed in image of the IDTs after the devices were released. Two separate devices were designed and fabricated due to the narrow bandwidth associated with the IDTs. Thus, one device was fabricated to demonstrate the down-converted mixed wave at $f_m = f_{c-s} = f_c - f_s$ (Device A) and the other one was fabricated to demonstrate the up-converted mixed wave at $f_m = f_{c+s} = f_c + f_s$ (Device B). For Device A, the carrier, signal, and mixed IDTs are designed to have a center frequency of 811 MHz, 460 MHz, and 360 MHz respectively. For Device B, the carrier, signal, and mixed IDTs have a center frequency of 587 MHz, 460 MHz, and 1043 MHz respectively. The spacing between the carrier and signal IDT is chosen that the carrier and signal wave will be in phase. Each of the IDTs are connected to three pads designed for ground-signal-ground (GSG) probes with a 150 μm pitch.

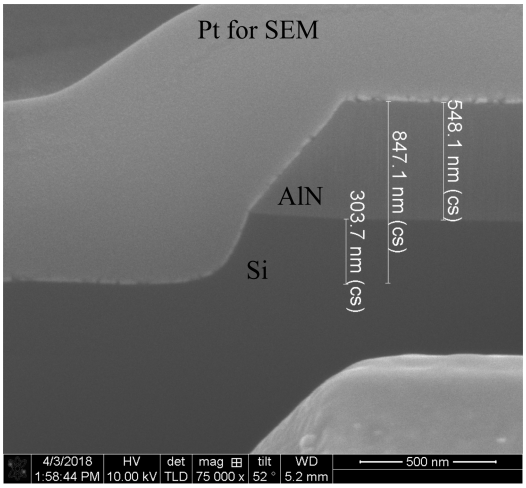

Figure 3.3: Scanning electron microscope image of the reactive ion etched Aluminum Nitride.

The Lamb wave devices were tested using a vector network analyzer (VNA) in two separate modes of operation. First, linear S-parameter experiments were conducted to determine the operating frequency, bandwidth, and impedance of each IDT set, and second, nonlinear conversion gain measurements were conducted to observe the parametric mixing effect. The linear measurements were essential for determining the operating frequency of the carrier IDT set, which requires a high input power. If the frequency of the carrier wave was not aligned with the resonant frequency of the IDT, the carrier wave would have been reflected, potentially damaging the power amplifier or VNA. The results and discussion of the linear measurements are

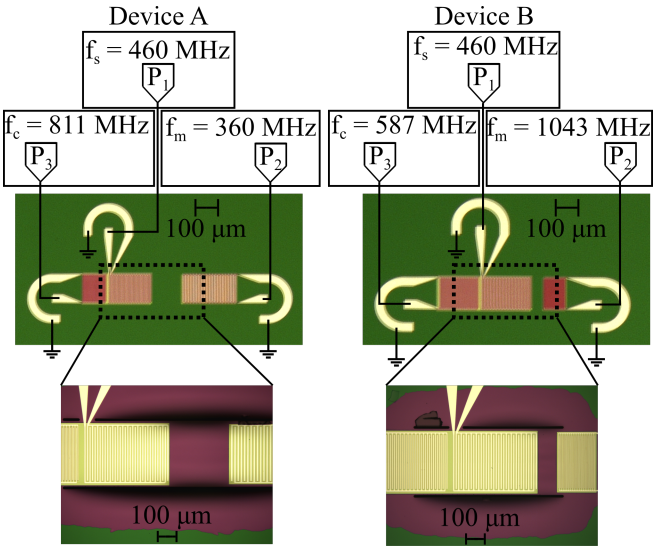

Figure 3.4: Optical images of the Lamb wave devices after fabrication. The top image is before the devices were released and the bottom image is after the devices were released.

detailed in the supplemental section. The measurement to observe the frequency mixing phenomenon was done using a VNA programmed in mixer mode. In this mode P_3 (carrier) had a monotone signal applied to it at f_c, the power level of the carrier wave (P_c) is varied from -5 dBm to +29 dBm. The frequency of the signal port P_1 was swept from 440 MHz to 480 MHz in 10 kHz steps with a constant power level (P_s) of -10 dBm. The receiving port P_2 measured the signal at either the down converted frequency ($f_m = f_c - f_s$) for Device A or the up converted frequency ($f_m = f_c + f_s$) for Device B. The VNA outputs data as the ratio of the power received at f_m to power delivered to the device at f_s and is termed the conversion factor (CF).

3.3 Circuit Model

Figure 3.5 shows the complete circuit model for the three-port nonlinear Lamb wave device. For this model, all the IDT fingers at the same port are modeled as one Modified Butterworth-Van Dyke (mBVD) model as opposed to each finger pair as is shown in Figure 3.1(c) [29, 30]. The ports are labeled as P_1(freq = f_s), P_2(freq = f_m), and P_3(freq = f_c) and correspond to the same ports used in the experiment. For this mBVD circuit, R^m, C^m, and L^m represent the motional resistance, capacitance, and inductance respectively. R^c, C^{idt}, and C^p represent

the static resistance, IDT capacitance, and parasitic capacitance respectively. As is with Figure 3.1, the subscripts in Figure 3.5 are used to indicate the IDT set (i.e., carrier, signal, and mixed). The mBVD models are connected to each other through lossy transmission lines labeled as TL_1 and TL_2. TL_1 and TL_1 are composed of n sets of inductor (L_{tl}), resistor (R_{tl}), and nonlinear capacitor (C_{nl}) unit cells. The number of unit cells is determined by the center-center distance between the IDT sets with 32 unit cells per acoustic wavelength. The values for the capacitor and inductor are calculated using 50 ohms as the TL characteristic impedance and the value for the resistor is fit using the measured S-parameters. The nonlinear capacitor changes its capacitance based on the voltage difference across its terminals. Thus, C_{nl} is defined as

$$C_{nl} = C_0 + \gamma V(x,t) \tag{3.1}$$

where γ is the modulation index, C_0 is the static capacitance, and V is the voltage as a function of time and space.

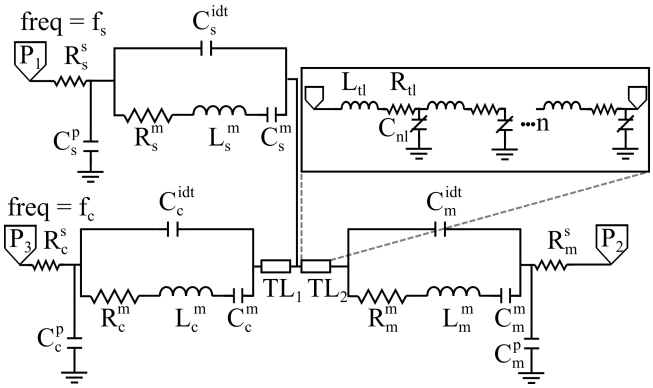

Figure 3.5: Circuit model consisting of 3 mBVD models connected through a nonlinear transmission line. The circuit model simulates the strain driven nonlinearity in AlN.

To determine the values of the motional arm circuit components of the mBVD model, equations are first used as initial guesses and then a nonlinear least-squares minimization algorithm is used to match the real and imaginary impedance of the mBVD model to the experimental device impedance. R^s is determined by experimental data while C^p and C^{idt} are calculated using the experimental data and Finite Element Analysis. The equations for the motional arm components are [30, 31]

$$C^m = \left(C^p + C^{idt}\right)\left[\left(\frac{f_{par}}{f_{ser}}\right)^2 - 1\right] \tag{3.2}$$

$$L^m = \frac{1}{2\pi f_{ser} C^m} \tag{3.3}$$

$$R^m = \frac{2\pi f_{ser}}{Q_{ser}} \tag{3.4}$$

where f_{par} and f_{ser} are the parallel and series resonant frequency respectively and Q_{ser} is the quality factor at the series resonant frequency. Table 3.1 shows the circuit parameters for the IDT sets for Device A and Device B after using the nonlinear least-squares minimization algorithm.

	Device A			Device B		
Circuit Parameter	Carrier	Signal	Mixed	Carrier	Signal	Mixed
$R^m(\Omega)$	63.93	79.35	95.46	69.76	79.35	84.19
C^m(fF)	24.51	39.29	52.23	31.94	39.29	17.83
L^m(nH)	1.57	3.08	3.76	2.30	3.08	1.31
C^p(pF)	1.41	2.36	2.89	1.93	2.42	0.90
C^{idt}(pF)	0.17	0.20	0.10	0.13	0.18	0.20
$R^s(\Omega)$	17.51	43.20	37.04	20.80	43.20	20.14

Table 3.1: Circuit parameters for the mBVD model.

3.4 Analytical Analysis

An analytic model was used to estimate the magnitude of acoustic parametric pumping in the AlN Lamb wave devices. The experiment consists of a thin plate with an out of plane dimension (thickness) much smaller than the acoustic wavelength yielding a system that can be approximated using the 1-D wave equation where displacements and stresses are primarily in the x-direction [26]. Additionally, the model assumes the AlN compliance varies linearly as a function of strain in the form of

$$S_p(x,t) = S_{p0} + \gamma\varepsilon(x,t) \tag{3.5}$$

Where γ is the slope of the compliance versus strain curve (i.e. modulation index) and S_{p0} is the static AlN's compliance. Assuming the strain varies sinusoidally, Equation 3.5 becomes

$$S_p(x,t) = S_{p0} + S_m \cos(\omega_c t - \beta_c x) \tag{3.6}$$

Where S_m is the amplitude of the compliance modulation, ω_c is the angular frequency of the compliance modulation, and β_c is the wave number. Substituting Equation 3.6 into the acoustic wave equation [26] produces signals at three different frequencies, the original signal frequency (f_s) and the two mixed frequencies ($f_m = f_c + f_s$ and $f_m = f_c - f_s$). Solving for the stress amplitudes at the mixed frequencies f_m yields

$$\sigma_{c-s}(x) = \frac{\sigma_0}{\sqrt{2}} \frac{\beta_c - \beta_s}{\beta_s} \sin\left(\frac{1}{2\sqrt{2}} \xi \beta_s x\right) \tag{3.7}$$

$$\sigma_{c+s}(x) = \frac{\sigma_0}{\sqrt{2}} \frac{\beta_c + \beta_s}{\beta_s} \sin\left(\frac{1}{2\sqrt{2}} \xi \beta_s x\right) \tag{3.8}$$

where σ_0 is the amplitude of the stress at frequency f_s and $\xi = \gamma\varepsilon/S_{p0} = S_m/S_{p0}$. A detailed derivation of these equations for a transmission line is presented in [12]. However, in the case presented here voltage is exchanged with stress and capacitance is exchanged with compliance. Other than these substitutions, the derivation is identical.

3.5 Results and Discussion

Figure 3.6 shows the experimental (solid black line) reflection coefficient (S_{ii}), where i is the port number, for Device A and the corresponding results from the mBVD circuit model (red dashed line). Figure 3.6(a), 3.6(b), and 3.6(c) show the reflection coefficient for the carrier, signal, and mixed IDTs respectively. The bottom left schematic shows the device and port numbers with an arrow pointing to the corresponding result. The carrier, signal, and mixed IDTs show dips in their S-parameters at frequencies of 811 MHz (-9 dB), 460 MHz (-7 dB), and 360 MHz (-6 dB) respectively. The dips in the reflection coefficient indicate the frequency

where the IDTs have the least amount of power reflected into the VNA. Each IDT set has a full width half max bandwidth of roughly 10 MHz. At the frequency where the reflection coefficient is the lowest (i.e. resonant frequency of the IDT), the AlN strains through the piezoelectric effect launching acoustic waves in the x-direction (Figure 3.1a). Accordingly, if an acoustic wave traveling at the resonant frequency of the IDT is present, the IDT will convert the acoustic wave to an electrical signal which will then be measured by the VNA. The results in Figure 3.6 indicate that each IDT is operating as designed for observing the nonlinear down-converted mixing effect predicted by the theory. Furthermore, the mBVD circuit model agrees well with the experimental results.

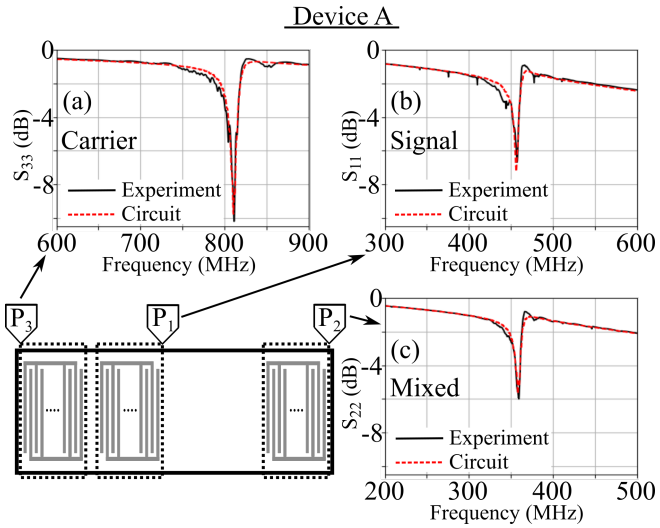

Figure 3.6: Reflection coefficient for the carrier, signal, and mixed IDTs for Device A. The solid black line are the measured results and the red dashed line are from the circuit model.

Figure 3.7 shows the experimental (solid black line) and mBVD model (dashed red line) reflection coefficients for the three IDT sets for Device B. The reflection coefficient is shown for the carrier, signal, and mixed IDTs in Figure 3.6(a), 3.6(b), and 3.6(c) respectively. The resonant frequencies for Device B are located at a carrier frequency of 587 MHz, signal frequency of 460 MHz, and mixed frequency of 1043 MHz, with values of -8 dB, -7 dB, and -6.5 dB. The bandwidths of the carrier and signal IDTs are $\approx$ 10 MHz, whereas the Mixed IDT has a bandwidth of $\approx$ 20 MHz. The results in Figure 3.6 can be interpreted the same way as the results in Figure 3.6 where dips in the S-parameters correspond to frequencies where electrical excitation of the IDTs launch and receive Lamb waves in the suspended AlN nitride plate. These experiment and modeling results also indicate that the IDT structure and circuit model for Device B

are working as designed for observing the nonlinear up-converted mixed signal.

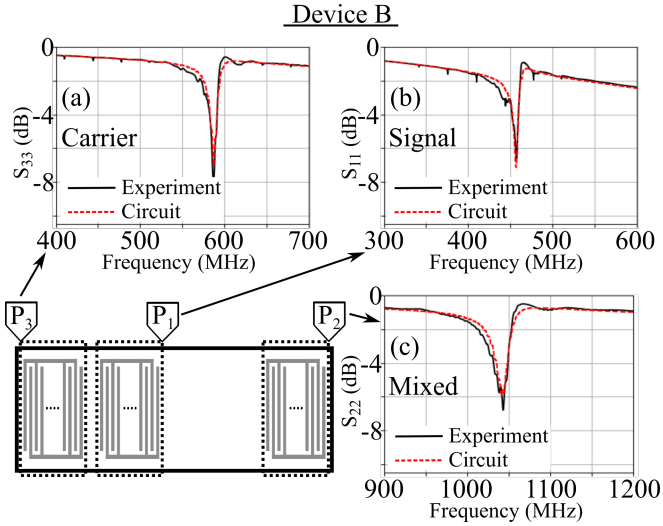

Figure 3.7: Reflection coefficient for the carrier, signal, and mixed IDTs for Device B. The solid black line are the measured results and the red dashed line are from the circuit model.

Figure 3.8 shows experimental (solid black line) and mBVD modeling (dashed red line) data of the conversion factor (CF) for Device A (i.e. frequency down-conversion device) as a function of frequency. This data is presented for three different carrier powers, P_c = -5, 0, and 5 dBm shown in Figure 3.8(a), 3.8(b), and 3.8(c) respectively. For the mBVD model, the modulation index (see Equation 1) was determined by fitting the circuit model to the experimental data. This value was used for all calculations and circuit models presented in this paper. For the experiment and mBVD model the carrier frequency (f_c) is set to 811 MHz while the signal frequency (f_s) is swept from 440 MHz to 480 MHz with a signal power of -10 dBm. In Figure 3.8(a) the CF, measured at the mixed frequency $f_m = f_c - f_s$, contains only noise from 331 MHz to 343 MHz because these frequencies are out of the signal and receive IDTs bandwidth. At 343 MHz the CF rises to a peak value at 350 MHz and varies within 5 dB until 365 MHz where the signal returns to the noise level. The 347-363 MHz response represents a frequency down-conversion from f_s to $f_c - f_s$ and has a $\approx$ 15 MHz full width half max (FWHM) bandwidth. The frequency down-conversion is caused by the nonlinear elastic compliance in the AlN waveguide, i.e. for a linear material frequency down-conversion would not occur and the CF would be at the noise floor. Additionally, as P_c increases from -5 dBm (Figure 3.8(a)) to 0 dBm (Figure 3.8(b)) and lastly 5 dBm (Figure 3.8(c)), the CF maintains its characteristic frequency dependence, however, the CF increases with increasing P_c due to an increase in

AlN compliance modulation. This increase in nonlinearity facilitates more power conversion to the side band frequencies, in the case show in Figure 3.8, the down-converted frequency. The mBVD circuit model (details in supplemental material) shows similar trends to the experimental data for all power levels apart from a distinct 10 dB dip at 358 MHz. This discrepancy is attributed to small device specific fluctuations due to fabrication that isn't captured by the mBVD model. These experimental results suggest acoustic filters and mixers can be combined into a single device due to the narrow bandwidth of the IDTs coupled with the nonlinearity of AlN. Thus, allowing for signal filtering and frequency conversion down to baseband to simultaneously occur in a single component rather than multiple components, as is currently done [12, 32].

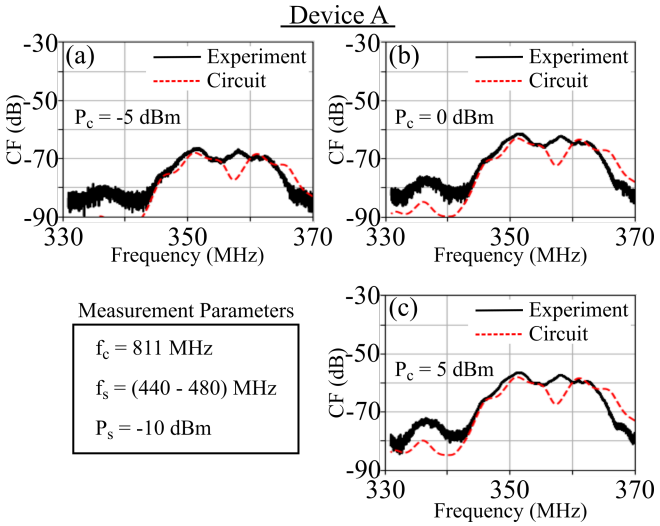

Figure 3.8: Experimental and modeling results of the conversion factor for Device A at three different carrier power levels. Starting from the top left and going clockwise, the carrier power is increased from -5 dBm to 0 dBm and lastly 5 dBm.

Figure 3.9 shows the experimental and the mBVD circuit model data for Device B, where f_c is 587 MHz and f_s is swept from 440 MHz to 480 MHz at -10 dBm for all P_c values. Note that Figure 4 demonstrates up-conversion ($f_c + f_s$), where Figure 3.8 frequency demonstrates down-conversion ($f_c - f_s$). The up-converted FWHM bandwidth is approximately 8 MHz starting at 1040 MHz and ending at 1048 MHz with the magnitudes of CF increasing with P_c (Figure 3.9a-c). However, the frequency response shape for Device B is different than Device A. Specifically, the receive IDT has a FWHM BW approximately two times larger than the other IDTs. This increase in the FWHM BW is also captured in the circuit model resulting in a close match

between model and experiment. The difference between the frequency response shapes in Figures 3.8 and 3.9 are attributed to the smaller dimensions required for Device B's receive IDT resulting in more imperfections, i.e. approaching the photolithographic resolution. Device B simultaneously facilitates signal filtering and frequency up-conversion through the narrowband IDTs and nonlinear AlN respectively.

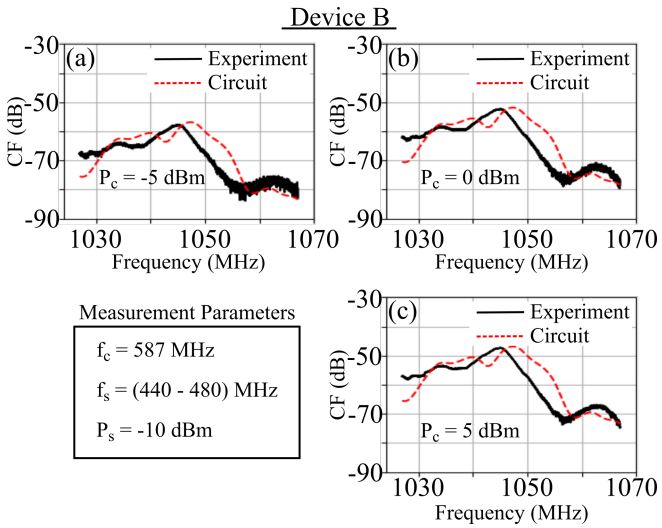

Figure 3.9: Conversion factor for Device B for three different power levels. Starting from the top left and going clockwise, the carrier power is increased from -5 dBm to 0 dBm and lastly 5 dBm.

Figure 3.10 shows the CF experimental data as a function of P_c for Device A (dots) and Device B (Triangles). Each data point represents the CF averaged over the frequency range defined by the full width half max. For both Device A and Device B, the plot shows a linear CF as a function of P_c for both devices at these power levels. However, the inset shows that in these devices, such as Device A, the CF becomes nonlinear and saturates at a P_c of $\approx$ 28 dBm. This saturation occurs because the AlN compliance saturates at this power level. Thus, further increasing P_c for these devices produces a negligible increase in CF. The maximum compliance modulation (ξ) for Device A at $P_c = 28$ dBm was estimated to be 2.8%, i.e. ξ is dependent on P_c. This compliance modulation value is close to the experimentally determined changes of AlN provided in previous publications [23]. Thus, these results indicate linear increases in CF as a function of power up to saturation of the compliance nonlinearities.

Figure 3.11 shows analytical calculations (Equations 3 and 4) of the center-to-center distance

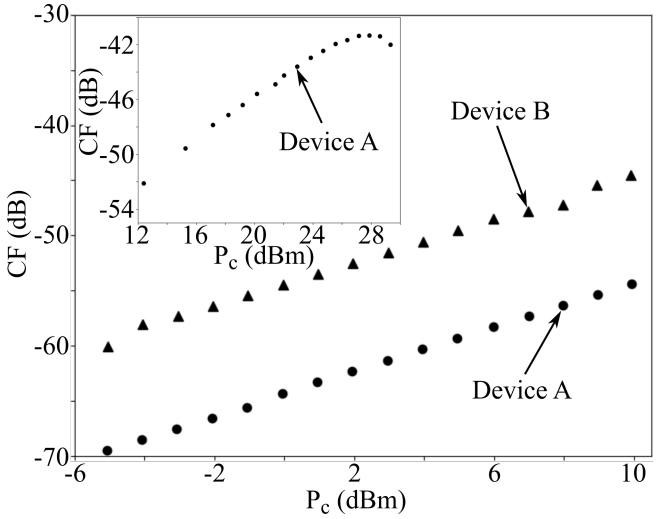

Figure 3.10: Conversion factor versus carrier power for Device A and Device B. The Inset shows the conversion factor versus carrier power for Device A at high carrier power.

between the signal IDT and the receive IDT (i.e. L_2 in Figure 3.1 necessary to achieve CF = 0 dB plotted as a function of f_c/f_s. For these calculations, f_s is held constant at 460 MHz and material nonlinearities of $\xi = 0.028$ (dotted lines) and $\xi = 0.20$ (solid lines) are investigated. A nonlinearity of 0.20 has been reported in FeGa alloys where a Delta-E effect produces large changes in compliance. All curves in Figure 3.11 show a decreasing L_2 as f_c increases. This length reduction can be explained by the additional wavelengths that are available at higher f_c for carrier and signal interactions (i.e. increasing f_c decreases the wavelength of the carrier signal). Focusing on the up-converted signal for (i.e. AlN) curve, L_2 begins at 0.24 mm for $f_c/f_s = 1$ and asymptotically approaches 0.0083 mm at large f_c. Regarding the down-converted signal, there is a restricted region below $f_c/f_s <\approx 2.4$ with the requirement that CF = 0 dB. Mathematically, this occurs through the appearance of an inverse Sine when the condition $f_c \geq f_s\left(\sqrt{2}+1\right)$ is met. This excluded frequency arises because there is insufficient power to satisfy the CF = 0 dB requirement for both up-converted and down-converted frequencies, arising from the fact that more power is transferred to the up-converted frequency [12, 33]. The two larger nonlinearity curves (i.e. $\xi = 0.20$) show similar trends to the dotted curves but with a dramatic reduction in device length across all frequencies due to the increased nonlinearity causing more power to be converted to both sidebands. Specifically, the device length (L_2) for both the up-converted and down-converted signals is reduced by 86% for all frequencies. These analytical results demonstrate that sub-millimeter sized single component acoustic frequency

mixers/filters that integrate passive and active elements are possible.

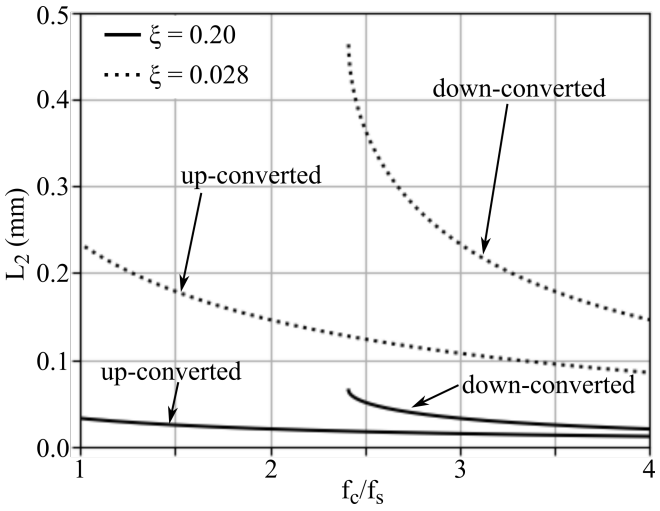

Figure 3.11: Analytical calculations of the device length required to achieve a 0 dB CF versus fc/fs. For these calculations fs is held constant 460 MHz and is held constant at 0.028.

3.6 Conclusion

Parametric coupling to facilitate frequency conversion in Lamb waves was experimentally demonstrated. Two devices were fabricated out of nonlinear piezoelectric aluminum nitride (AlN), one to demonstrate frequency up-conversion and one to demonstrate frequency down-conversion. Two interdigitated transducers (IDTs) was used to generate a high-power carrier wave and a low-power signal wave while an additional IDT were used receive the frequency converted mixed wave. Each device was first tested to determine the operating frequency of the IDTs followed by nonlinear measurements to observe the frequency conversion effect. The power level of the carrier wave is swept from -5 dBm to 28 dBm where the higher power increases the nonlinearity in the AlN. The Lamb wave devices were modeled using a circuit and closely match the experimental results. Lastly, an analytical model was used to demonstrate optimal device performance and dimensions showing that sub-millimeter sized single component acoustic frequency mixers/filters that integrate passive and active elements are possible. This research demonstrates that a properly designed acoustic time varying transmission lines (TVTLs) can be a solution to reducing the size of a traditional electromagnetic TVTLs.

3.7 Chapter References

[1] P. K. Tien, "Parametric amplification and frequency mixing in propagating circuits", Journal of Applied Physics **29**, 1347 (1958).

[2] P. K. Tien and H. Suhl, "A Traveling-Wave Ferromagnetic Amplifier", Proceedings of the IRE **46**, 700 (1958).

[3] C. W. Peterson, W. A. Benalcazar, M. Lin, T. L. Hughes, and G. Bahl, "Strong nonreciprocity in modulated resonator chains through synthetic electric and magnetic fields", Physical Review Letters **123**, 63901 (2019).

[4] A. Kord, D. L. Sounas, and A. Alu, "Pseudo-Linear Time-Invariant Magnetless Circulators Based on Differential Spatiotemporal Modulation of Resonant Junctions", IEEE Transactions on Microwave Theory and Techniques **66**, 2731 (2018).

[5] A. Kord, D. L. Sounas, and A. Alu, "Magnet-Less Circulators Based on Spatiotemporal Modulation of Bandstop Filters in a Delta Topology", IEEE Transactions on Microwave Theory and Techniques **66**, 911 (2018).

[6] A. Kord, M. Tymchenko, D. L. Sounas, H. Krishnaswamy, and A. Alu, "CMOS Integrated Magnetless Circulators Based on Spatiotemporal Modulation Angular-Momentum Biasing", IEEE Transactions on Microwave Theory and Techniques **67**, 2649 (2019).

[7] N. A. Estep, D. L. Sounas, J. Soric, and A. Alù, "Magnetic-free non-reciprocity and isolation based on parametrically modulated coupled-resonator loops", Nature Physics **10**, 923 (2014).

[8] M. Biedka, Q. Wu, X. Zou, S. Qin, and Y. E. Wang, "Integrated time-varying electromagnetic devices for ultra-wide band nonreciprocity", IEEE Radio and Wireless Symposium, RWS **2018-January**, 80 (2018).

[9] X. Zou, Q. Wu, and Y. E. Wang, "Parametrically enhanced delay line with monolithically integrated time-varying transmission lines (TVTL)", IEEE Radio and Wireless Symposium, RWS, 1 (2019).

[10] Q. Wu, X. Zou, R. Zhu, and Y. E. Wang, "Chip-Scale RF Correlator with Monolithically Integrated Time-Varying Transmission Line (TVTL)", IEEE MTT-S International Microwave Symposium Digest **2018-June**, 431 (2018).

[11] W. H. Louisell, "Coupled Mode and Parametric Electronics", Students Quarterly Journal **32**, 57 (1961).

[12] S. Qin, Q. Xu, and Y. E. Wang, "Nonreciprocal components with distributedly modulated capacitors", IEEE Transactions on Microwave Theory and Techniques **62**, 2260 (2014).

[13] X. Zou, Q. Wu, and Y. E. Wang, "Monolithically Integrated Parametric Mixers with Time-varying Transmission Lines (TVTL)", IEEE MTT-S International Microwave Symposium Digest **2019-June**, 971 (2019).

[14] A. L. Cullen, *A Travelling-Wave Parametric Amplifier*, 1958.

[15] A. L. Cullen, "THEORY OF THE TRAVELLING-WAVE PARAMETRIC AMPLIFIER By Professor A. L. CULLEN, Ph.D., Member.", Iee, 101 (1959).

[16] S. Qin and Y. E. Wang, "Parametric conversion with distributedly modulated capacitors (DMC) for low-noise and non-reciprocal RF front-ends", IEEE MTT-S International Microwave Symposium Digest, 0 (2013).

[17] J. P. Domann and G. P. Carman, "Strain powered antennas", Journal of Applied Physics **121**, 44905 (2017).

[18] Z. Yao, Y. E. Wang, S. Keller, G. P. Carman, S. S. Member, Y. E. Wang, S. S. Member, S. Keller, and G. P. Carman, "Bulk Acoustic Wave-Mediated Multiferroic Antennas: Architecture and Performance Bound", IEEE Transactions on Antennas and Propagation **63**, 3335 (2015).

[19] J. D. Schneider, J. P. Domann, M. K. Panduranga, S. Tiwari, P. Shirazi, Z. Yao, C. Sennott, D. Shahan, S. Selvin, G. McKnight, W. Wall, R. N. Candler, Y. E. Wang, and G. P. Carman, "Experimental demonstration and operating principles of a multiferroic antenna", Journal of Applied Physics **126**, 10.1063/1.5126047 (2019).

[20] G. Chao, "Parametric amplification of surface acoustic waves", Applied Physics Letters **16**, 399 (1970).

[21] A. J. Bahr, "Reflection and Amplification of Acoustic Surface Waves by Interdigital Transducers with Active Circuit Loading", IEEE Transactions on Microwave Theory and Techniques **18**, 642 (1970).

[22] W. P. Robbins, "Pump Requirements for Parametric Amplification and Generation of Surface Waves on YZ LiNbO¡inf¿3¡/inf¿", IEEE Transactions on Sonics and Ultrasonics **22**, 257 (1975).

[23] E. Defaÿ, N. Ben Hassine, P. Emery, G. Parat, J. Abergel, and A. Devos, "Tunability of aluminum nitride acoustic resonators: A phenomenological approach", IEEE Transactions on Ultrasonics, Ferroelectrics, and Frequency Control **58**, 2516 (2011).

[24] D. S. Shim and D. A. Feld, "A general nonlinear Mason model of arbitrary nonlinearities in apiezoelectric film", Proceedings - IEEE Ultrasonics Symposium, 295 (2010).

[25] D. A. Feld and D. S. Shim, "Determination of the nonlinear physical constants in a piezoelectric AlNfilm", Proceedings - IEEE Ultrasonics Symposium, 277 (2010).

[26] A. K. Mal and S. J. Singh, *Deformation of Elastic Solids* (Prentice Hall, 1991).

[27] T. Ikeda, *Fundamentals of Piezoelectricity*, Oxford science publications (Oxford University Press, 1996).

[28] C. Campbell, *Surface Acoustic Wave Devices and Their Signal Processing Applications* (Academic Press, INC., San Diego, 1989), p. 484.

[29] C. M. Lin, V. Yantchev, J. Zou, Y. Y. Chen, and A. P. Pisano, "Micromachined one-port aluminum nitride lamb wave resonators utilizing the lowest-order symmetric mode", Journal of Microelectromechanical Systems **23**, 78 (2014).

[30] Y. Wang, W. L. Goh, K. T. Chai, X. Mu, Y. Hong, P. Kropelnicki, and M. Je, "Parasitic analysis and π-type Butterworth-Van Dyke model for complementary-metal-oxide-semiconductor Lamb wave resonator with accurate two-port Y-parameter characterizations", Review of Scientific Instruments **87**, 1 (2016).

[31] I. S. Uzunov, M. D. Terzieva, B. M. Nikolova, and D. G. Gaydazhiev, "Extraction of modified butterworth - Van Dyke model of FBAR based on FEM analysis", 2017 26th International Scientific Conference Electronics, ET 2017 - Proceedings **2017-Janua**, 1 (2017).

[32] D. M. Pozar, *Microwave Engineering*, 4th (John Wiley & Sons, Inc., Hoboken, 2012).

[33] J. M. Manley and H. E. Rowe, "Some general properties of nonlinear elements. I. General energy relations", Proceedings of the Institute of Radio Engineers **44**, 904 (1956).

4 Voltage-Controlled Ferromagnetic Resonance of Dipole-Coupled CoFeB Nanoellipses

4.1 Introduction

Tunable RF filters, with the ability to broaden and shift operation frequency, are an essential component for flexible RF front ends [1, 2]. Such frequency-agile filters provide the capability for reprogrammable devices that shift signal processing from application specific hardware (e.g., ASIC's) to software-based solutions such as software defined radio (SDR) [3, 4]. Current RF filters are primarily surface acoustic wave (SAW) and bulk acoustic wave (BAW) devices due to their high quality factor (Q) and linear response. Consequently, due to the electro-mechanical nature of these filters, most of the proposals for filter tuning involve materials with electric field dependent elastic properties (i.e., stiffness) [3]. However, the voltage required to generate a sufficient tuning electric field for a 10 MHz shift of the passband is often quite large [5].One possible solution for larger tunability is to take advantage of ferromagnetic resonance [6] as a bandpass filter and use magnetoelasticity [7] as the tuning mechanism. Such a coupled approach can be achieved using multiferroic heterostructures.

The excitation and manipulation of magnetization using multiferroic materials has recently gained substantial interest due to their applications in memory [8–10], logic [11–13], nano-biotechnology [14, 15], and radio frequency (antenna) components [16–19]. Specifically, strain powered multiferroics provide the promise of low power consumption. For example, non-volatile magnetic memory storage can be realized by using strain to deterministically control the magnetization orientation in ferromagnetic nanoelements [8, 10, 20, 21]. The potential to harness this energy efficiency in the context of RF electronics was also demonstrated by using

strain generated from a piezoelectric substrate to manipulate the easy axis in a magnetostrictive material, causing spin waves to vary their propagation characteristics [22]. Similarly, dipole coupling in nanodot arrays has been manipulated via voltage-induced strain to create a binary logic wire, signifying the potential to modify electromagnetic coupling mechanisms directly. Dipole coupled nickel disks have also been investigated for their potential to produce artificial ferromagnet and antiferromagnet ordering in synthetic multiferroics [11]. Furthermore, dynamic manipulation of magnetization in a multiferroic has been shown to be useful for antenna applications due to elimination of the platform effect [16–18].

Leveraging the nonsymmetric properties of the permeability tensor, along with the field tunability of resonance properties of magnetic materials, numerous RF devices can be made with magnetic materials such as frequency modulators, Faraday-rotation isolators, phase shifters, and microwave power limiters, all of which require a magnetic bias field for operation and tunability [23]. Typically, ferrites are used for such devices, but these materials often lack the magnetostrictive properties which are often present in magnetoelastic materials. In this paper, a tunable filter is investigated that modifies the resonant and dipole modes of a nanodot array via magnetoelastic interactions in a multiferroic composite.

4.2 Device Fabrication

Our design for controlling ferromagnetic resonance (FMR) spectra consists of elliptical magnetoelastic CoFeB islands on a piezoelectric substrate as shown in Figure 4.1(a). The ellipse material was chosen as CoFeB because of its large saturation magnetization and reasonable magnetostriction in comparison to other magnetoelastic materials such as Ni. Specifically, this is expected to offer larger tunability of the ferromagnetic resonance frequency due to increased dipole coupling and strain response. This design uses voltage-induced strains in the piezoelectric layer to introduce a magnetoelastic anisotropy that changes the resonance of the nanostructures. The magnetoelastic elements are numerically studied with a Landau-Lifshitz-Gilbert

(LLG) micromagnetic formulation [24]:

$$\frac{\partial \underline{m}}{\partial t} = -\mu_0 \gamma \left(\underline{m} \times \underline{H}_{eff}\right) + \alpha \left(\underline{m} \times \frac{\partial \underline{m}}{\partial t}\right) \tag{4.1}$$

where μ_0 is the permeability of free space, γ is the gyromagnetic ratio, and α is the Gilbert damping constant. The model neglects thermal fluctuations and assumes small elastic deformations as well as uniform strains within the magnetoelastic elements [24, 25]. In Equation 4.1, the effective magnetic field ($\underline{H}_{eff}$) for the system is the sum of the exchange field ($\underline{H}_{ex}$), demagnetization field ($\underline{H}_{d}$), and magnetoelastic field ($\underline{H}_{me}$). The magnetoelastic field is defined by $\underline{H}_{me} = 3\lambda_s Y\left(\varepsilon_x - \varepsilon_y\right)/\mu_0 M_s$ where λ_s is the saturation magnetostriction, Y is the Young's modulus, M_s is the saturation magnetization, and (ε_x, ε_y) are the voltage induced strains in the x and y directions respectively. The biaxial strain difference can be produced experimentally by applying an electric field to patterned electrodes on the piezoelectric layer. The $\underline{H}_{me}$ term is represented in Equation 4.1 by a uniform uniaxial anisotropy defined as $K = \mu_0 M_s \underline{H}_{me}/2$ [24, 26]. The LLG formulation is solved with finite difference approach using a Dormand-Prince finite difference method [27, 28].

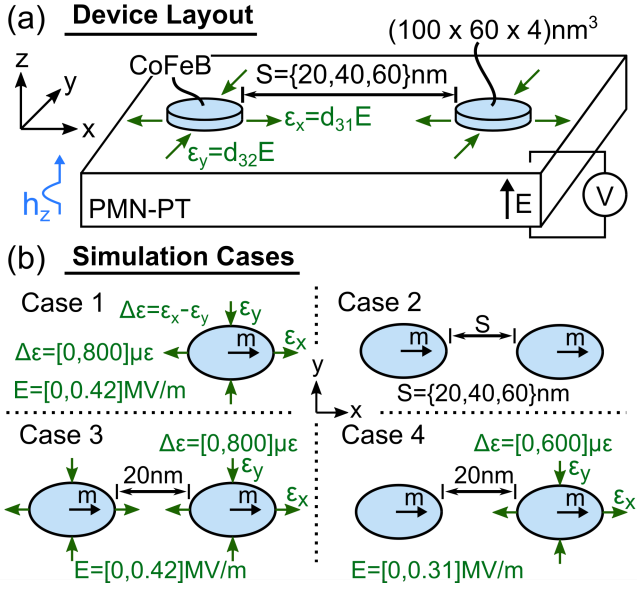

Figure 4.1: Ellipse geometry for micromagnetic simulation. Applied Gaussian pulse magnetic field is directed through the thickness of the ellipse.

To probe the FMR properties of the magnetoelastic ellipses, the magnetization is first allowed to reach an equilibrium state and then a magnetic Gaussian pulse (hz) is applied through the

element thickness (z-axis). To reduce simulation time, the Gilbert damping constant is set to $\alpha_e = 0.3$ until an equilibrium state is reached. This typically takes approximately 2 ns of simulation time and once the equilibrium state is reached the Gilbert damping constants is returned to the actual material value. The process of starting the code with an artificially high α_e dramatically decreases the simulation time required to reach the equilibrium state without influencing the spin dynamics reorientation during the simulation [8, 14]. For the dynamic regime, the damping parameter is then set to a more realistic value of $\alpha = 0.015$ [24] and the volume averaged magnetization $\mathbf{m}(t)$ of each nanostructure is recorded at uniform time intervals of 1 ps for another 4.1 ns of simulation time. The excitation field distribution in time is given by:

$$h_z(t) = Ae^{-\frac{4log(2)}{w^2}(t-b)^2} \tag{4.2}$$

where A is the peak height of the pulse, w is the full width at half maximum (FWHM) of the peak, b is the center of the peak, and t is time. This type of pulse is chosen because it is often used in experiment [29] and provides a significant broadband excitation of at least 20 GHz which enables subsequent calculation of the magnetic susceptibility (χ) up to this frequency (i.e., in a range that is suitable for typical device applications). The applied pulse is spatially uniform through the volume of the ellipses with a small 20 Oe amplitude chosen to minimize nonlinear behavior. Based on the choice of excitation field, the susceptibility in the frequency domain can be found from $M_z(\omega) = X(\omega) \cdot H(\omega)$ [30] by performing a Fast Fourier Transform (FFT) on the volume averaged $m_z(t)$. Here, the pulse parameters are: $A = 20$ Oe, $w = 10$ ps, and $b = 20$ ps.

In this paper, the FMR response of the magnetoelastic ellipse configurations shown in Figure 4.1(b) are studied with an applied voltage-induced biaxial strain and, in a second case, when one ellipse is dipole-coupled to a single neighbor. The biaxial strain state ($\Delta\varepsilon$) is given by $\Delta\varepsilon = \varepsilon_x - \varepsilon_y$ and is chosen with a tensile strain (ε_x) directed along the x-axis and a compressive strain (ε_y) directed along the y-axis. This type of strain state is typical for strain-mediated multiferroics, and can be experimentally achieved by applying an electric field (E) through the thickness of a single crystal PMN-PT substrate, as shown in Figure 4.1(b). In such cases, the

corresponding strain values can be calculated from $\varepsilon_x = d_{31}E$ and $\varepsilon_y = d_{32}E$, where $d_{31} = 771$ pm/V and $d_{32} = -1147$ pm/V are the piezoelectric coefficients of the PMN-PT substrate. Furthermore, Finite element studies calculating the voltage-induced strain distribution in a PMN-PT substrate with closely patterned nanomagnets were conducted and indicate a highly localized strain is achievable. Specifically, patterned electrodes were used to localize the strain to a single ellipse with neighboring elements experiencing less than 6% of this strain. Hence, the use of a localized strain in the micromagnetic simulations of dipole coupled ellipses is a reasonable approximation. Similar patterned electrodes have been utilized to generate localized strain in various magnetic nanostructures [10, 21, 25]. Using these voltage-induced biaxial strains, the FMR properties of the ellipses are studied in four cases, as shown in Figure 4.1(b). Case 1 involves a single ellipse subjected to a biaxial strain that varies between 0 $\mu\varepsilon$ and 800 $\mu\varepsilon$ in 200 $\mu\varepsilon$ intervals corresponding to applied electric fields between 0 MV/m and 0.42 MV/m for 500 micron thick PMN-PT. Case 2 focuses on two dipole-coupled ellipses which are unstrained and have edge-to-edge separation distances of 20 nm, 40 nm, and 60 nm. Case 3 has two dipole-coupled ellipses with a separation distance of 20 nm subjected to equal biaxial strains equal to those in the first case. Finally, Case 4 involves two dipole-coupled ellipses separated by 20 nm, but with strain applied only to one of the ellipses, with strains ranging from 0 $\mu\varepsilon$ and 600 $\mu\varepsilon$ in 200 $\mu\varepsilon$, corresponding to applied electric fields between 0 MV/m and 0.31 MV/m.

The simulated ellipse geometry is 100 nm x 60 nm x 4 nm for all cases. The dimensions and aspect ratio were chosen to ensure the ellipses were in a single domain state with shape anisotropy sufficient to keep the magnetization directed in-plane along the major axis. This choice was made because such self-biasing would be advantageous in future device applications since it removes the requirement for an external magnetic bias field. Furthermore, with the material and geometries chosen for the simulation, all of the modeled nanodots would be thermally stable in experiment, with a shape anisotropy-induced energy well of 70 KbT (i.e., larger than the 40 KbT required for modern MRAM devices) [10]. All of the above-mentioned geometries were numerically simulated using a mesh with cubic elements (1 nm^3) and with the material properties for CoFeB, as given in Table 4.1 [24, 31, 32]. Furthermore, the mesh was

verified by using the built-in function edgesmooth that produced results similar to the results without edgesmooth. This result indicates that the solution has converged to the actual solution dictated by a smooth geometry.

Material Property	Symbol	Units	Value
Saturation Magnetization	M_s	A/m	1.3×10^6
Gilbert Damping (equilibrium state)	α_e	-	0.3
Gilbert Damping (dynamic regime)	α	-	0.015
Exchange Stiffness	A_{ex}	J/m	1.2×10^6

Table 4.1: Material properties for CoFeB nanoellipses.

4.3 Results and Discussion

Figures 4.2(a)-4.2(e) show the FMR response of a single CoFeB ellipse when a voltage-induced biaxial strain is applied. Figure 4.2(a) shows the susceptibility along the z-axis of the CoFeB ellipse as a function of frequency for electric fields of 0 MV/m to 0.42 MV/m. As seen from the figure, the susceptibility exhibits two peaks which are designated as bulk and edge modes. Specifically, the largest peak is the bulk mode and the secondary peak is the edge mode. As the strain is increased, both the bulk and edge modes shift up in frequency by similar amounts. For example, at 0.10 MV/m the bulk mode frequency is 7.32 GHz and the edge mode frequency is 12.45 GHz. Increasing the electric field to 0.31 MV/m results in bulk and edge mode frequencies of 7.81 GHz and 12.93 GHz, respectively. Figures 4.2(b)-4.2(e) show the dynamics of mz for two bulk modes (P1, P3) and two edge modes (P2, P4) of the ellipse. These mode shapes are shown for the modes P1 = 6.84 GHz and P2 = 12.21 GHz, when the system is unstrained, and for P3 = 7.81 GHz and P4 = 12.93 GHz when the system is strained by applying 0.31 MV/m to the PMN-PT substrate The mode shapes shown were selected after reviewing the entire dynamic images of the spin excitations. The snapshots selected best convey the resonance values and were obtained at approximately a quarter of a period. Specifically, this quarter period time interval corresponds with the peaks of a sinusoidal magnetic driving field with the same frequency. So, for example, the magnetic state for the peak at 6.84 GHz is recorded at

time intervals of 36 ps while a 6.84 GHz low amplitude driving field simultaneously excites this system. Each mode shape image is then color normalized by a maximum RGB value that corresponds to the maximum magnitude of m_z. Since the maximum value of mz is different for each image, the normalization factor is also unique, meaning that the colors in each image cannot be compared directly. Instead the mode shapes are intended only to show general trends regarding the location of standing wave nodes, as this is sufficient to show the strain-induced mode modulation that is the focus of this paper. From Figure 4.2, it is clear that the mode shapes for P1 and P3 are similar, while the mode shapes of P2 and P4 are similar.

The large peak in the susceptibility is from the bulk magnetization, while the small peak is due to demagnetization effect along the periphery of the ellipse. Since the small peak is due to the demagnetization effect, the position and shape of the small peak would change if the aspect ratio is changed. The voltage-induced changes in the single CoFeB ellipse's susceptibility values (Figure 24.2) are explained using the magnetoelastic response of the nanostructure. The applied electric field results in tensile and compressive strains directed along the major and minor axes of the ellipse, respectively. Since CoFeB is a positive magnetoelastic material, the applied strains cause the magnetization to favor orientation along the major axis of the ellipse. This effectively makes the major axis magnetically stiffer resulting in a higher ferromagnetic resonance frequency observed as the peaks shifting to the right with increasing electric field (i.e., strain). This is analogous to a mechanical spring-mass system in which the natural frequency increases with spring stiffness. This analogy can be further understood by considering the Kittel Equation:

$$\omega = \gamma\mu_0\sqrt{\left((N_x - N_z)M_x - H_{eff}\right)\left((N_y - N_z)M_x - H_{eff}\right)} \tag{4.3}$$

where ω is the ferromagnetic resonance frequency, the effective field (H_{eff}) is the effective field due to mechanical strain, and the N_i are the demagnetization factors along the x-, y-, and z-axes, respectively. For the geometry used in this paper, $N_x \approx 0.046$, $N_y \approx 0.078$, and $N_z \approx 0.875$. Comparison between simulation and calculation of FMR, using the above relation, shows a strong agreement. For example, at an applied electric field of 0.42 MV/m, the

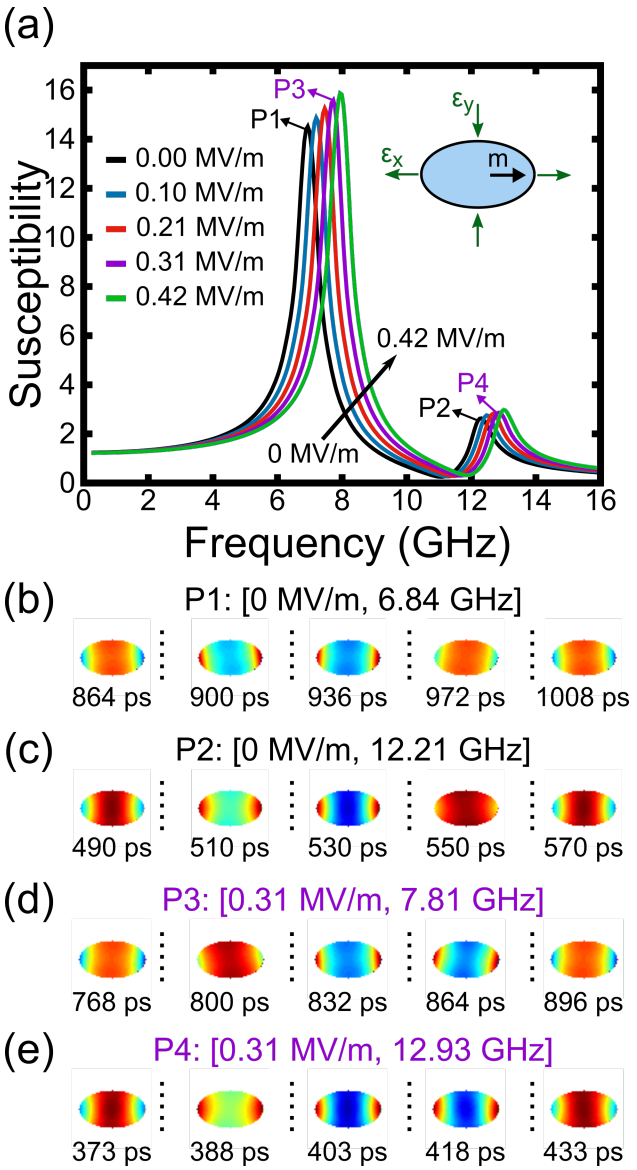

Figure 4.2: (a) Susceptibility of CoFeB ellipse when subjected to voltage-induced biaxial strain. Magnetic excitation is generated by Gaussian pulse magnetic field directed through the thickness of the ellipse. (b)-(e) Normalized mode shapes generated by simulation software for peaks P1-P4.

simulation predicts a resonance of 8.03 GHz while the calculation results in 8.05 GHz. Similar agreement is found for the other applied electric fields with 1.4% being the largest error between simulation and experiment for an applied electric field of 0.21 MV/m.

Figures 4.3(a)-4.3(d) show the FMR response changes of two dipole coupled CoFeB ellipses as their separation distance (S) increases from 20 nm to 60 nm. Figure 4.3(a) shows the susceptibility of the dipole coupled ellipses as a function of frequency. In this case, the susceptibility is determined by taking the FFT of the volume averaged magnetic z-component $m_z(t)$ of the dipole-coupled system. In contrast to the single ellipse case, Figure 4.3(a) shows that at 20 nm separation the dipole coupled system exhibits three resonance peaks. Inspection of the plot shows that the largest and smallest peaks resemble the bulk and edge modes in the single ellipse case, while the peak labeled D2 is new. When the separation is increased to 40 nm, it is seen that the new D2 peak is reduced to a small bump near 7.9 GHz and ultimately disappears once the separation distance is 60 nm. Figures 4.3(b)-4.3(d) show the mode shapes of the dipole coupled system at frequencies D1 = 7.08 GHz, D2 = 8.54 GHz, and D3 = 12.45 GHz for 60 nm, 20 nm, and 60 nm separation distances, respectively. The mode shapes were obtained using the same method as in the single ellipse case. The mode shapes for peaks D1 and D3 resemble the bulk and edge mode shape for the single ellipse case, respectively. The mode shape for D2 does not resemble any of the single ellipse mode shapes and exhibits an anti-aligned shape. The observed splitting of the dipole mode is similar to the mode splitting seen in other coupled resonators used in RF filters, such as MEMS, electromagnetic, and surface acoustic wave resonators [33–38]. This is shown by the alternating regions of dark and light colors within the central region of the ellipses in Figure 4.3(c).

The effects of separation distance on the FMR spectra of two dipole-coupled ellipses are explained by the strength of the dipole coupling between the two magnetoelastic elements. In particular, as the separation distance increases, the dipole-coupling necessarily decreases nonlinearly. Given this inherent decrease in coupling strength with separation distance, it follows that past some critical distance, there is effectively no dipole coupling between the ellipses.

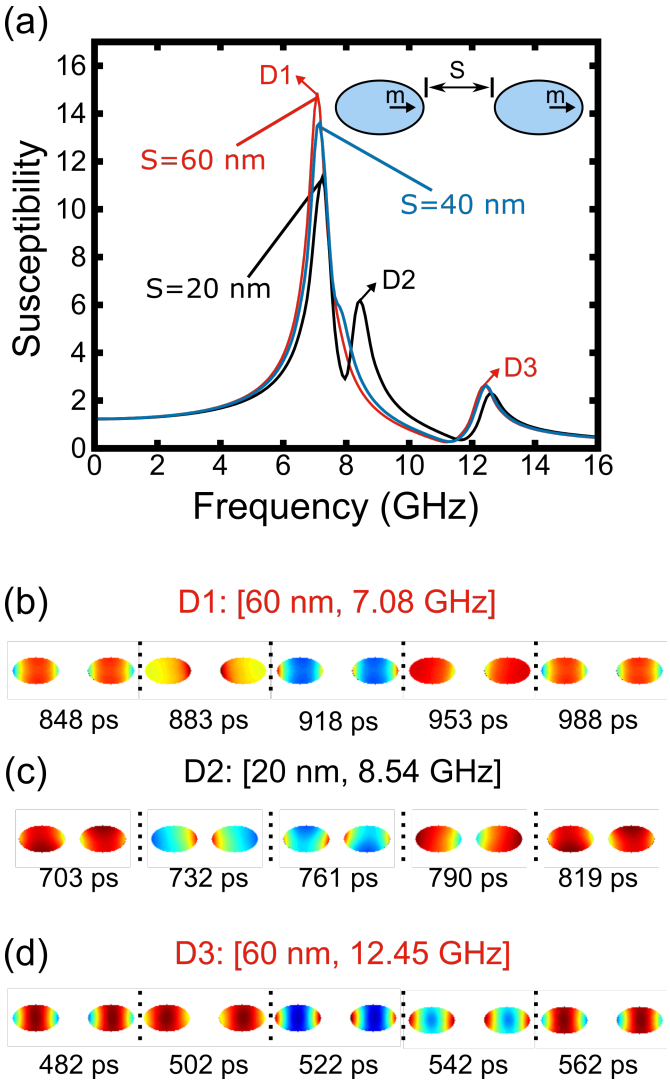

Figure 4.3: (a) Susceptibility of two dipole coupled CoFeB ellipses for separation distances S = 20, 40, 60 nm. (b)-(d) Normalized mode shapes generated by simulation software for peaks D1-D3.

Past this critical distance, there would effectively be two isolated magnetoelastic elements and an FMR response similar to the single ellipse case would be expected. Thus, the peak labeled D2 is no longer present resulting in an increased susceptibility at the primary frequency. This trend is exactly what the simulations show because the third peak (D2) is present for the 20 nm separation distance and gradually disappears until the separation reaches 60 nm where the FMR spectra has only two-peaks centered almost exactly at the frequencies of the single ellipse case.

Figure 4.4 shows the FMR response changes of two dipole-coupled elements separated by 20 nm when a voltage-induced biaxial strain is applied to both ellipses. The two ellipses are subjected to the same applied electric field (i.e., same strain state) and the electric field is varied from 0.00 MV/m to 0.42 MV/m. The susceptibility exhibits three peaks and, as the electric field is increased, each peak shifts up in frequency equally. For example, when the electric field is increased from 0.10 MV/m to 0.31 MV/m the three resonance peaks increase from 7.56, 8.54, 12.69 GHz to 8.05, 9.03, 13.18 GHz. Lastly, the largest, middle, and smallest peaks correspond to the bulk, dipole, and edge modes.

The FMR changes for the dipole-coupled ellipses separated by 20 nm (Figure 4.4) and subjected to equal voltage-induced biaxial strains are caused by the previously discussed strain and dipole effects. Specifically, the appearance of a third (middle) peak for these FMR responses is a consequence of the strong dipole coupling at 20 nm seen in the previous simulations. Furthermore, the shift of the resonance curves with increased electric field is explained by the Kittel equation for the single ellipse case. It is interesting to note that the combined effect of strain and dipole-coupling appear as a superposition of the two effects. This is reasonable since the model assumptions imply the studied system is linear in terms of mechanics (i.e., linear magnetoelasticity) and also follows linear magnetization dynamics (i.e., due to the small angle of magnetization precession).

Figure 4.5 shows the FMR response changes of two dipole coupled ellipses varies when a

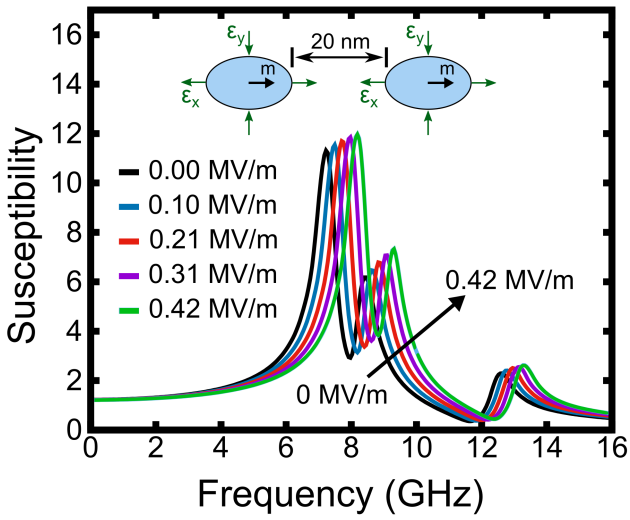

Figure 4.4: Susceptibility of the dipole-coupled ellipses separated by 20 nm and subjected to different electric fields (i.e. strains).

voltage-induced biaxial strain is applied to only one of the structures. In this case, the separation distance is chosen as 20 nm and the electric field is varied from 0.00 MV/m to 0.31 MV/m. For 0 applied electric field, the susceptibility exhibits only three resonance peaks and the bulk mode is identified by the diamond shaped marker on the plot. Similarly, only three resonance peaks occur for 0.10 MV/m and the bulk mode is identified by the triangular marker. At 0.21 MV/m four resonance peaks are seen and a square marker is used to identify the bulk mode at this electric field. Inspection of the inset shows that the first three resonance peaks occur at 7.08 GHz, 7.56 GHz, and 8.78 GHz while the edge mode peak occurs at 12.93 GHz. At 0.31 MV/m, a fifth resonance peak appears near the edge mode. The five resonances for this case occur at 7.08 GHz, 8.05 GHz, 9.03 GHz, 12.45 GHz, and 13.83 GHz.

Like the previous simulation case, a combined effect of mechanics and dipole-coupling explains the changes in FMR spectra for the two-magnet system with voltage-induced biaxial strain applied to only one element (Figure 4.5. Without an applied electric field, the expected three-peak spectra is obtained since only dipole coupling is present. When the electric field is increased to 0.10 MV/m still three peaks are present, but there is a slight shift consistent with increasing field. The first (bulk) mode is centered at 7.3 GHz which is the same value as the single ellipse case at that applied field. Notably, the first peak is slightly broadened in compar-

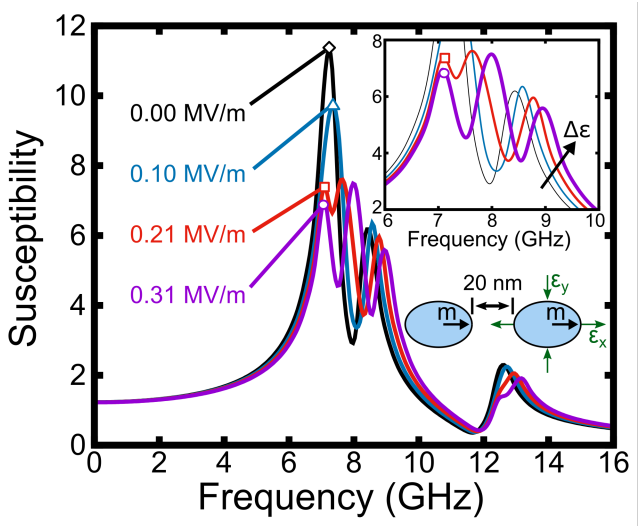

Figure 4.5: Susceptibility of the dipole-coupled ellipses separated by 20 nm with only one ellipse subjected to the different electric fields (i.e. strains).

ison to the no applied electric field case. This results from the superposition of the mechanical and dipole effects previously discussed. Specifically, in the previous simulation case, the bulk mode frequency for the unstrained dipole system was 7.08 GHz. Due to superposition, this peak is not lost in the case of Figure 4.5, but instead combines with the 7.3 GHz peak resulting in the broadened bulk mode of the 0.10 MV/m response. As the electric field is increased to 0.21 MV/m, a separation between these two peaks is seen. Specifically, there is still a 7.08 GHz peak corresponding to the unstrained dipole bulk mode while the second peak is further shifted to 7.56 GHz (matching the corresponding single ellipse case at 0.21 MV/m). Consequently, the appearance of a fourth peak is a result of causing a large enough distinction between the FMR responses of the individual strained and unstrained ellipses. Similarly, this superposition of the individual FMR peaks of each ellipse explains the response at 0.31 MV/m. The additional consequence is that there is now sufficient separation between the edge mode peaks of the strained and unstrained ellipses such that a fifth distinct peak appears. Based on these results, it is reasonable to speculate that increasing the number of dipole coupled elements and trying different strain combinations would increase the number of peaks and increase the tunability of FMR. Thus, opening the possibility for new strain-based filtering, antenna, or computing devices that rely on RF operating principles.

4.4 Conclusion

The results demonstrate large tunability of ferromagnetic resonance spectra with applied voltage induced strain. Specifically, the resonance peaks were shown to be deterministically shifted with applied strain. Furthermore, combining the effects of strain with dipole coupling leads to significant modulation of the FMR spectra. For example, simulation indicated the combination of dipole coupling with strain not only shifts resonance peaks, but also introduces new ones in the two magnet systems. Lastly, the results open avenues for further investigation regarding increasing the number of coupled elements and varying combinations of strain for future strain-based filtering, antenna, or computing device applications such as software defined radio.

4.5 Chapter References

[1] K.-y. Hashimoto and T. Kimura, "Tunable RF SAW / BAW Filters : What are Possible and What are Not ?", 8522.

[2] J. F. Luy, T. Mueller, T. Mack, and A. Terzis, "Configurable RF receiver architectures", IEEE Microwave Magazine **5**, 75 (2004).

[3] R. Aigner, "Tunable Filters? Reality Check Foreseeable Trends in System Architecture for Tunable RF Filters", IEEE Microwave Magazine **16**, 82 (2015).

[4] S. Gevorgian, A. Tagantsev, and A. K. Vorobiev, *Tuneable Film Bulk Acoustic Wave Resonators*, edited by B. Derby (Springer-Verlag London, 2013).

[5] A. Noeth, P. Muralt, A. K. Tagantsev, N. Setter, and T. Yamada, "Tunable Thin Film Bulk Acoustic Wave Resonator Based on Ba¡sub¿x¡/sub¿Si¡sub¿1-x¡/sub¿TiO¡sub¿3¡/sub¿ Thin Film", IEEE Transactions on Ultrasonics, Ferroelectrics, and Frequency Control **57**, 379 (2010).

[6] C. Kittel, "On the theory of ferromagnetic resonance absorption", Physical Review **73**, 155 (1948).

[7] S. Chikazumi, *Physics of Ferromagnetism*, Vol. 1, International Series of Monographs on Physics 11 (Oxford University Press, Oxford, 1997), p. 655.

[8] C.-Y. Y. Liang, S. M. Keller, A. E. Sepulveda, A. Bur, W.-Y. Y. Sun, K. Wetzlar, and G. P. Carman, "Modeling of magnetoelastic nanostructures with a fully coupled mechanical-micromagnetic model", Nanotechnology **25**, 435701 (2014).

[9] J. Xu, C. M. Leung, X. Zhuang, J. Li, S. Bhardwaj, J. Volakis, and D. Viehland, "A low frequency mechanical transmitter based on magnetoelectric heterostructures operated at their resonance frequency", Sensors (Switzerland) **19**, 10.3390/s19040853 (2019).

[10] Q. Wang, X. Li, C.-Y. Y. Liang, A. Barra, J. Domann, C. Lynch, A. Sepulveda, and G. Carman, "Strain-mediated 180° switching in CoFeB and Terfenol-D nanodots with perpendicular magnetic anisotropy", Applied Physics Letters **110**, 102903 (2017).

[11] A. C. Chavez, W. Y. Sun, J. Atulasimha, K. L. Wang, and G. P. Carman, "Voltage induced artificial ferromagnetic-antiferromagnetic ordering in synthetic multiferroics", Journal of Applied Physics **122**, 10.1063/1.4997612 (2017).

[12] A. C. Chavez, A. Barra, and G. P. Carman, "Voltage control of magnetic monopoles in artificial spin ice", Journal of Physics D: Applied Physics **51**, 10.1088/1361-6463/aac0ae (2018).

[13] R. Lo Conte, Z. Xiao, C. Chen, C. V. Stan, J. Gorchon, A. El-Ghazaly, M. E. Nowakowski, H. Sohn, A. Pattabi, A. Scholl, N. Tamura, A. Sepulveda, G. P. Carman, R. N. Candler, and J. Bokor, "Influence of Nonuniform Micron-Scale Strain Distributions on the Electrical Reorientation of Magnetic Microstructures in a Composite Multiferroic Heterostructure", Nano Letters **18**, 1952 (2018).

[14] Z. Xiao, R. Lo Conte, C. Chen, C.-Y. Liang, A. Sepulveda, J. Bokor, G. P. Carman, and R. N. Candler, "Bi-directional coupling in strain-mediated multiferroic heterostructures with magnetic domains and domain wall motion", Scientific Reports **8**, 5207 (2018).

[15] Z. Xiao, K. P. Mohanchandra, R. Lo Conte, C. Ty Karaba, J. D. Schneider, A. Chavez, S. Tiwari, H. Sohn, M. E. Nowakowski, A. Scholl, S. H. Tolbert, J. Bokor, G. P. Carman, and R. N. Candler, "Enhanced magnetoelectric coupling in a composite multiferroic system via interposing a thin film polymer", AIP Advances **8**, 55907 (2018).

[16] Z. Yao, Y. E. Wang, S. Keller, G. P. Carman, S. S. Member, Y. E. Wang, S. S. Member, S. Keller, and G. P. Carman, "Bulk Acoustic Wave-Mediated Multiferroic Antennas: Architecture and Performance Bound", IEEE Transactions on Antennas and Propagation **63**, 3335 (2015).

[17] J. P. Domann and G. P. Carman, "Strain powered antennas", Journal of Applied Physics **121**, 44905 (2017).

[18] T. Nan, H. Lin, Y. Gao, A. Matyushov, G. Yu, H. Chen, N. Sun, S. Wei, Z. Wang, M. Li, X. Wang, A. Belkessam, R. Guo, B. Chen, J. Zhou, Z. Qian, Y. Hui, M. Rinaldi, M. E. McConney, B. M. Howe, Z. Hu, J. G. Jones, G. J. Brown, and N. X. Sun, "Acoustically actuated ultra-compact NEMS magnetoelectric antennas", Nature Communications **8**, 1 (2017).

[19] X. Yang, Y. Gao, J. Wu, Z. Zhou, S. Beguhn, T. Nan, and N. X. Sun, "Voltage tunable multiferroic phase shifter with YIG/PMN-PT heterostructure", IEEE Microwave and Wireless Components Letters **24**, 191 (2014).

[20] A. A. Kundu, A. C. Chavez, S. M. Keller, G. P. Carman, and C. S. Lynch, "360° deterministic magnetization rotation in a three-ellipse magnetoelectric heterostructure", Journal of Applied Physics **123**, 104105 (2018).

[21] A. Barra, J. Domann, K. W. Kim, and G. Carman, "Voltage Control of Antiferromagnetic Phases at Near-Terahertz Frequencies", Physical Review Applied **9**, 34017 (2018).

[22] M. Balinskiy, A. C. Chavez, A. Barra, H. Chiang, G. P. Carman, and A. Khitun, "Magnetoelectric Spin Wave Modulator Based on Synthetic Multiferroic Structure", Scientific Reports **8**, 1 (2018).

[23] D. M. Pozar, *Microwave Engineering*, 4th (John Wiley & Sons, Inc., Hoboken, 2012).

[24] I. Gilbert, A. C. Chavez, D. T. Pierce, J. Unguris, W.-Y. Y. Sun, C.-Y. Y. Liang, and G. P. Carman, "Magnetic microscopy and simulation of strain-mediated control of magnetization in PMN-PT/Ni nanostructures", Applied Physics Letters **109**, 162404 (2016).

[25] J. Cui, C.-Y. Liang, E. A. Paisley, A. Sepulveda, J. F. Ihlefeld, G. P. Carman, and C. S. Lynch, "Generation of localized strain in a thin film piezoelectric to control individual magnetoelectric heterostructures", Applied Physics Letters **107**, 92903 (2015).

[26] B. D. Cullity and C. Graham, *Introduction to Magnetic Materials*, 2nd (Wiley, New York, 2009).

[27] A. Vansteenkiste and B. Van de Wiele, "MuMax: A new high-performance micromagnetic simulation tool", Journal of Magnetism and Magnetic Materials **323**, 2585 (2011).

[28] A. Vansteenkiste, J. Leliaert, M. Dvornik, M. Helsen, F. Garcia-Sanchez, and B. Van Waeyenberge, "The design and verification of MuMax3", AIP Advances **4**, 107133 (2014).

[29] B. B. Maranville, R. D. McMichael, S. A. Kim, W. L. Johnson, C. A. Ross, and J. Y. Cheng, "Characterization of magnetic properties at edges by edge-mode dynamics", Journal of Applied Physics **99**, 97 (2006).

[30] R. D. McMichael and M. D. Stiles, "Magnetic normal modes of nanoelements", Journal of Applied Physics **97**, 10J901 (2005).

[31] C. Burrowes, N. Vernier, J.-P. Adam, L. Herrera Diez, K. Garcia, I. Barisic, G. Agnus, S. Eimer, J.-V. Kim, T. Devolder, A. Lamperti, R. Mantovan, B. Ockert, E. E. Fullerton, and D. Ravelosona, "Low depinning fields in Ta-CoFeB-MgO ultrathin films with perpendicular magnetic anisotropy", Applied Physics Letters **103**, 182401 (2013).

[32] X. Liu, W. Zhang, M. J. Carter, and G. Xiao, "Ferromagnetic resonance and damping properties of CoFeB thin films as free layers in MgO-based magnetic tunnel junctions", Journal of Applied Physics **110**, 33910 (2011).

[33] S. A. Bhave, D. Gao, R. Maboudian, and R. T. Howe, "Fully-differential poly-SiC Lame mode resonator and checkerboard filter", in 18th ieee international conference on micro electro mechanical systems, 2005. mems 2005. (2005), pp. 223–226.

[34] G. Endoh, M. Ueda, O. Kawachi, and Y. Fujiwara, "High performance balanced type SAW filters in the range of 900 MHz and 1.9 GHz", Proceedings of the IEEE Ultrasonics Symposium **1**, 41 (1997).

[35] J.-s. Hong and M. J. Lancaster, “Cross-Coupled Microstrip Hairpin-Resonator Filters”, **46**, 118 (1998).

[36] T. Morita, Y. Watanabe, M. Tanaka, and Y. Nakazawa, “Wideband low loss double mode SAW filters”, 95 (2003).

[37] C. T. Nguyen, “Frequency-selective MEMS for miniaturized low-power communication devices”, IEEE Transactions on Microwave Theory and Techniques **47**, 1486 (1999).

[38] P. Gay-Balmaz and O. J. Martin, “Electromagnetic resonances in individual and coupled split-ring resonators”, Journal of Applied Physics **92**, 2929 (2002).

5 Conclusion

This dissertation proposes three concepts that solve relevant problems and challenges in the realm of communication technology. The challenges addressed are low frequency communication in RF-denied media such as seawater, integrating mixers and filters into a single acoustic component for RF front ends, and solving the need for tunable filters for wideband radio, cognitive radio, and software defined radio. Specifically, solutions involving acoustics and strain mediated control of magnetism were investigated to reduce dimensions and remove the requirement for an external magnetic bias field. Strain mediated control of magnetism was accomplished through the use of multiferroic heterostructures where a piezoelectric material applies a strain to a magnetostrictive ferromagnet thus changing the ferromagnet's magnetization. The change in magnetization can be used to wirelessly communicate information as well as adjust the ferromagnet's high frequency susceptibility for RF filter applications.

In Chapter 2 strain control of magnetism was investigated for use in low frequency communication in RF-denied media. First an analytical model was developed to demonstrate the advantage of using a magnetic dipole over an electric dipole. Next, an experimental test setup utilizing the multiferroic effect to control magnetism with an applied strain is developed. Results showed that a strain can be used to dynamically control magnetization resulting in a dynamic magnetic near field that can be used to transmit information. The results were compared to analytical model and closely match the experimental results. Lastly, the analytical model was used to demonstrate that a multiferroic antenna can be used to generate time varying magnetic fields with magnitudes of 1 fT at a km away from the antenna using approximately 5 cm^3 of magnetic material.

In Chapter 3 acoustic waves in aluminum nitride (AlN) were investigated to create an integrated mixer and filter. Specifically, Lamb waves at two different frequencies were simultaneously launched in a suspended thin film of AlN using interdigitated transducers (IDTs). One wave is a high-power wave responsible for creating a time and space varying mechanical compliance

and the other is a low-power information carrying signal wave. The waves were filtered through the IDTs and mixed through the nonlinearity in AlN producing up and down converted waves. The up and down converted waves were detected using an additional IDT. Results showed the ability to create a single device with the ability to filter and mix a signal, thus, integrating mixers and filters into the acoustic domain.

In Chapter 4 strain mediated tuning of the ferromagnetic susceptibility in dipole coupled single domain ellipses was investigated. Tuning the susceptibility facilitates the tuning of band-pass or band-stop filters which are essential for cognitive radio and software defined radio. The susceptibility is tuned using a strain applied through an electric field induced deformation in piezoelectric PMN-PT as opposed to a applied magnetic bias field. The results showed a tuning of approximately 2 GHz if two ellipses are strain and a broadening of the band pass when only one ellipse is strained. These results show the potential for using magnetic materials to facility frequency tuning in modern RF front ends.

This dissertation looked at next generation acoustic and magnetic devices for RF communication. The magnetic devices rely on a dynamic strain, as opposed to an applied magnetic field (Oersted field). Using a mechanical strain takes advantage of the relatively slow acoustic wave velocity, thus, reducing the size of devices. Furthermore, magnetic materials of three specific advantages for communication purposes: (1) their susceptibility can be tuned over a wide range; (2) they offer more efficient communication in lossy RF-denied media such as seawater when compared to an electric based antenna; and (3) they have nonreciprocal signal transmission due to their material properties. Additionally, taking advantage of the mechanical nonlinearity in some materials, mixers and filters can be integrated into a single component, thus, moving one step closer to an all acoustic RF front end. The author hopes that the advancements discussed in this dissertation will lead to further technological developments for future communication devices.